

A GNAR-Based Framework for Spectral Estimation of Network Time Series: Application to Global Bank Network Connectedness

Cristian F. Jiménez-Varón¹, Marina I. Knight¹

October 8, 2025

Abstract

Patterns of dependence in financial networks, such as global bank connectedness, evolve over time and across frequencies. Analysing these systems requires statistical tools that jointly capture temporal dynamics and the underlying network topology. This work develops a novel spectral analysis framework for Generalized Network Autoregressive (GNAR) processes, modeling dependencies beyond direct neighbours by incorporating r -stage neighbourhood effects, unlike existing methods that at best rely solely on adjacency-based interactions. We define the GNAR spectral density and related quantities, such as coherence and partial coherence, for which we propose both parametric and network-penalized nonparametric estimators. Extensive simulations demonstrate the strong performance of the parametric spectral estimator, as also backed up by theoretical arguments. The proposed framework has wide applications, and here we focus on the analysis of global bank network connectedness. The findings illustrate how the GNAR spectral quantities effectively capture the frequency-specific cross-nodal dependencies, thus yielding estimates consistent with established measures, while also uncovering richer temporal and structural patterns of volatility transmission.

Key words: Autoregressive processes, Bank network connectedness, Network data, Spectral estimation, Time series.

¹Department of Mathematics. University of York. E-mail: cristian.jimenezvaron@york.ac.uk; marina.knight@york.ac.uk

1 Introduction

Understanding the structural interconnections among financial institutions—particularly banks—is fundamental for assessing systemic risk and ensuring financial stability. Financial systems are inherently interacting: institutions are linked through credit exposures, liquidity provision, derivative contracts, and overlapping asset holdings. These structural relationships give rise to a network topology underlying financial markets, which governs the transmission and amplification of shocks. While connectedness measures have become a central concept in financial econometrics (Diebold and Yilmaz, 2009, 2014), they can be interpreted more generally as empirical summaries of the underlying network architecture of financial interdependence (Demirer et al., 2018; Wu et al., 2020; Gabauer et al., 2023).

A substantial body of literature has focused on modeling connectedness in the time domain. The framework of Diebold and Yilmaz (2009, 2014) uses forecast error variance decompositions from vector autoregressive (VAR) models to quantify spillovers in returns or volatilities, generating a network of interdependencies. High-dimensional extensions employ regularization techniques, such as Lasso, to identify sparse structures and isolate dominant channels of risk propagation (Demirer et al., 2018). While powerful, these approaches tend to aggregate dynamic behavior over time, masking the possibility that spillovers may operate differently over various time horizons. Recognizing this limitation, Baruník and Křehlík (2018) proposed a spectral-domain connectedness framework that decomposes variance contributions across frequency bands. This enables a richer characterization of short-, medium-, and long-term dynamics in volatility transmission. Yet, the majority of connectedness studies, including spectral approaches, still operate under the assumption of vector-valued time series without explicitly modeling the network structure among the components. What remains underdeveloped is a modeling paradigm that directly incorporates known network topologies into the frequency-domain analysis of financial systems.

Beyond the specific application to finance, network time series data have gained growing attention across fields such as neuroscience, systems biology, and econometrics. In these contexts, measurements are collected at the nodes of a graph and evolve over time, leading to time-indexed observations constrained by a network topology. Such settings demand statistical models that jointly account for temporal and cross-nodal dependencies (Lauritzen, 1996; Friedman et al., 2007; Songsiri et al., 2009; Dahlhaus, 2000).

The Generalized Network Autoregressive (GNAR) model introduced by Knight et al. (2020) provides a flexible and interpretable framework for modeling time series on networks. Central to this development is the incorporation of both temporal and topological dependencies by regressing the time series at each node on past values from itself and its (r -edges away, also known as r -stage) neighbors. The GNAR model is particularly attractive in high-dimensional applications due to its capacity to impose sparsity through the network structure while maintaining scalability. In this context, recent developments have also provided much needed time-domain tools such as network (partial) autocorrelation measures (Nason et al., 2025).

What is currently missing from the current literature, and forms the focus of this work, is a frequency-domain modeling framework that naturally accounts for the network topology: here we respond to this challenge by defining and estimating the spectral density matrix for a GNAR process, thereby enabling the analysis of frequency-specific dependencies over the network via (partial) coherence measures. Unlike

classical multivariate spectral techniques (Brillinger, 2001; Brockwell and Davis, 1991; Shumway and Stoffer, 2017), our approach for both parametric and nonparametric spectral estimation explicitly leverages network topology, allowing for richer interpretations of how signals propagate across nodes at different frequencies.

Although related efforts exist (Loukas and Perraudeau, 2019) that propose a spectral framework based on joint time-vertex stationarity using tools from graph signal processing, these approaches rely on different structural assumptions. Specifically, they typically assume fixed graph Laplacians and restrict interactions to immediate neighbors. In contrast, the GNAR model accommodates more general r -stage neighborhood interactions, making it more suitable for capturing indirect dependencies and multi-step transmission effects.

Spectral estimation for network time series presents a range of methodological challenges. First, the high dimensionality of the data—arising from a large number of nodes and potential interactions—necessitates the use of regularization techniques to ensure computational feasibility and statistical reliability. Second, spectral analysis naturally involves complex-valued spectral density and precision matrices, thus limiting the direct applicability of standard tools such as the graphical Lasso introduced by Hastie et al. (2009). These methods typically begin with the estimation of a covariance or precision matrix and are designed for real-valued data. When the underlying network topology is only partially known or completely unknown, incorporating structural assumptions into estimation leads to what is referred to as covariance selection problems (Dempster, 1972; Lauritzen, 1996), where sparsity is imposed to reflect prior beliefs about possible connections in the graph. However, these classical approaches are not immediately applicable in the spectral domain due to the complex-valued nature of frequency-domain objects. Recent developments, such as the complex graphical Lasso proposed by Deb et al. (2024), address this issue by constructing an isomorphism between complex-valued Hermitian matrices and real-valued representations, thereby enabling the inference of network structures in the frequency domain.

By contrast, in this work we assume a known network structure and propose a spectral estimation framework for the GNAR model that directly incorporates the network topology. In the spirit of classical spectral analysis, we develop both parametric and nonparametric estimators while still accounting for the network structure. Our estimators allow the inclusion of r -step neighborhood information, thus accommodating both direct and indirect temporal-spatial dependencies. This integration of network constraints into spectral analysis yields a flexible and interpretable methodology suited for complex, high-dimensional network time series data, which will be shown to be superior to classical network spectral estimation via VAR modeling.

This paper is organised as follows. Section 2 introduces a graphical model viewpoint of the GNAR model and sets the scene for defining the GNAR spectral density and introducing both parametric and nonparametric estimators in Section 3. Section 4 evaluates the empirical performance of our spectral estimation methods through extensive simulations. In Section 5 we illustrate the utility of our proposed framework through an application to global bank network connectedness data from Demirer et al. (2018). Using our proposed network-informed GNAR spectral estimators, we investigate the frequency-specific patterns of connectedness among financial institutions across different countries and regions. This analysis reveals underlying structures of systemic risk and provides new insights into how inter-bank dependence relationships vary across global financial networks.

2 Brief review of network time series modelling framework

Key to our developments, in this section we outline the main properties of generalized network autoregressive (GNAR) models of [Knight et al. \(2020\)](#), primarily through their connection to vector autoregressive (VAR) models ([Lütkepohl, 2005](#)), and then establish their connection to graphical models for time series.

2.1 The GNAR model

[Knight et al. \(2020\)](#) introduce GNAR models as a way to capture temporal dependence while also exploiting the available network structure. A *network time series* $X := (\mathbf{X}_t, G)$ is a stochastic process consisting of a multivariate time series $\{\mathbf{X}_t\}_t \in \mathbb{R}^d$ recorded over the vertices (nodes) of an underlying network $G = (K, E)$. Here, G is an undirected static graph with K denoting the set of d nodes, and $E \subseteq K \times K$ its set of edges. The distance between any pair of nodes (i, j) is denoted by $\delta(i, j)$, and is given by the length of the shortest path between them. Typical for the graph theory literature, an adjacency matrix $\mathbf{A} \in \{0, 1\}^{d \times d}$ encodes the direct interactions among pairs of nodes in the graph G , with a 1 marking each edge.

Each univariate time series $\{X_{i,t}\}_t \in \mathbb{R}$ is associated with a node $i \in K$, and central to GNAR modelling is the concept of r -stage neighbours of node i , denoted by $\mathcal{N}_r(i)$. This essentially encompasses nodes that are on a path of length $r = 1, \dots, r_{\max}$ from node i , where $r_{\max} \in \mathbb{N}$ represents the length of the longest shortest path in G , ensuring that the distance between any pair of nodes (i, j) satisfies $\delta(i, j) \leq r_{\max}$. Intimately connected to the r -stage neighbourhood concept, [Nason et al. \(2025\)](#) also introduce a sequence of adjacency matrices $\{\mathbf{A}_r\}_{r \geq 1} \in \{0, 1\}^{d \times d}$. Simply put, the r -stage adjacency matrix \mathbf{A}_r is populated with 1's for node pairs that are r -stage neighbours, and $\mathbf{A}_1 := \mathbf{A}$.

A GNAR model incorporates not only *node-wise autoregression*, standard for VAR formulation, but also *neighborhood regression*. Specifically, the evolution of each nodal time series $\{X_{i,t}\}$ is influenced by its own (p) past values, and by a weighted linear combination $\{Z_{i,t}^r\}$ of its r -stage neighbours time series, namely

$$Z_{i,t}^r = \sum_{j \in \mathcal{N}_r(i)} w_{ij} X_{j,t},$$

where w_{ij} denotes the weight assigned to the connection between the neighbouring nodes i and j .

Throughout this work, we follow the compact notation introduced by [Nason et al. \(2025\)](#). The node-wise representation of a GNAR model for the process X with maximum lag $p \in \mathbb{N}$ and maximum r -stage depth $s_k \in \{1, \dots, r_{\max}\}$ at each lag is denoted as $\text{GNAR}(p, [s_1, \dots, s_p])$ and given by

$$X_{i,t} = \sum_{k=1}^p \left(\alpha_k X_{i,t-k} + \sum_{r=1}^{s_k} \beta_{kr} Z_{i,t-k}^r \right) + u_{i,t}, \quad (1)$$

where $\alpha_k \in \mathbb{R}$ are the standard autoregressive parameters, $\beta_{kr} \in \mathbb{R}$ are the neighbourhood autoregressive parameters for $r = 1, \dots, s_k$ at each lag $k = 1, \dots, p$, and $\{u_{i,t}\}_t$ are independent and identically distributed (IID) white noise terms with mean zero and variance $\sigma^2 > 0$ for all nodes i .

The GNAR model in (1) admits a compact vectorized representation across the node set,

$$\mathbf{X}_t = \sum_{k=1}^p \left(\alpha_k \mathbf{X}_{t-k} + \sum_{r=1}^{s_k} \beta_{kr} \mathbf{Z}_{t-k}^r \right) + \mathbf{u}_t, \text{ where,} \quad (2)$$

$$\mathbf{Z}_t^r = (\mathbf{W} \odot \mathbf{A}_r) \mathbf{X}_t. \quad (3)$$

In the above, $\mathbf{A}_r \in \{0, 1\}^{d \times d}$ is the r -stage adjacency matrix, $\mathbf{W} \in \mathbb{R}^{d \times d}$ is the weights matrix (see Definitions 1 and 2 in [Nason et al. \(2025\)](#)), and \odot denotes the Hadamard (element-wise) product. The noise term $\{\mathbf{u}_t\}$ follows a multivariate white noise process with mean zero and covariance matrix $\sigma^2 \mathbb{I}_d$.

GNAR as constrained VAR. [Knight et al. \(2020\)](#) show that the GNAR model can be rewritten as a constrained VAR model and leveraged this connection to establish stationarity conditions for GNAR processes over a static network. The VAR coefficients, $\{\Phi_k\}_{k=1}^p$ in the notation of [Lütkepohl \(2005\)](#), explicitly incorporate the network-based restrictions

$$\Phi_k = \alpha_k \mathbb{I}_d + \sum_{r=1}^{s_k} \beta_{kr} (\mathbf{W} \odot \mathbf{A}_r). \quad (4)$$

Theorem 2.1 (Stationarity of GNAR ([Knight et al., 2020](#))). *Let $\{\mathbf{X}_t\}$ be a global- α GNAR($p, [s_1, \dots, s_p]$) process with an associated static network G . Then $\{\mathbf{X}_t\}$ is stationary if the coefficients in (2) satisfy*

$$\sum_{k=1}^p \left(|\alpha_k| + \sum_{r=1}^{s_k} |\beta_{kr}| \right) < 1.$$

A practically significant advantage of GNAR models is their parsimonious nature. Unlike traditional VAR models where the number of parameters to estimate increases with both dimensionality d and autoregressive order p , the number of GNAR parameters primarily depends on the depth of the r -stage neighborhood regression and on the maximum lag. For example, a global- α GNAR($p, [s_1, \dots, s_p]$) model contains only p autoregressive coefficients (α_k) and ($\sum_{k=1}^p s_k$) neighborhood regression coefficients (β_{kr}), in contrast to a VAR(p) model that requires estimating pd^2 parameters. Therefore, as long as $q := p + \sum_{k=1}^p s_k < pd^2$, the GNAR model in (2) requires significantly fewer parameters, highlighting its advantage over traditional VAR models. This reduction in complexity is especially beneficial in real-world applications where pd^2 often exceeds the number of available time steps, with the efficient GNAR parameterisation offering a practical approach for high-dimensional time series that enables clear interpretation of estimated interactions.

GNAR model estimation. As discussed in previous works ([Leeming, 2019](#); [Knight et al., 2020](#); [Nason et al., 2025](#)), GNAR parameter estimation can be formulated by expressing the GNAR process as a linear model fitted by ordinary least squares. Assume that $T \in \mathbb{N}$ time steps of (stationary) data $\mathbf{X} := [\mathbf{X}_1, \dots, \mathbf{X}_T]$ arise from a GNAR process of known order $(p, [s_1, \dots, s_k])$ ([Knight et al. \(2020\)](#) Section 3.1 discusses order selection in GNAR models) and the aim is to estimate the coefficients $\{\alpha_k\}_k$ and $\{\beta_{kr}\}_{k,r}$ in model (2). If $\mathbf{y}_t := \mathbf{X}_t \in \mathbb{R}^d$ is the data vector of responses and $\mathbf{X}_t := [\mathbf{X}_{t-1}, \mathbf{Z}_{t-1}^{1:s_1}, \dots, \mathbf{X}_{t-p}, \mathbf{Z}_{t-p}^{1:s_1}] \in \mathbb{R}^{d \times q}$ the design matrix at time t for the coefficient vector $\boldsymbol{\beta} := (\alpha_1, \beta_{11}, \dots, \beta_{1s_1}, \alpha_2, \dots, \beta_{ps_p}) \in \mathbb{R}^q$, where $\mathbf{Z}_{t-1}^{1:s_1} :=$

$[\mathbf{Z}_{t-1}^1, \dots, \mathbf{Z}_{t-1}^{s_1}]$ as in (3), the GNAR model (2) can be rewritten as $\mathbf{y}_t = \mathbf{X}_t \boldsymbol{\beta} + \mathbf{u}_t$ with observations assumed to be uncorrelated and \mathbf{u}_t defined for $t = p+1, \dots, T$.

Denoting by $n = T-p$ the number of observations for which there are p prior lags available for estimation, and concatenating the responses \mathbf{y}_t into a single column vector $\mathbb{Y} \in \mathbb{R}^{nd}$ and the design matrices \mathbf{X}_t into a single matrix $\mathbb{X} \in \mathbb{R}^{nd \times q}$, the linear model provides the framework for estimating the GNAR parameters $\boldsymbol{\beta}$ via least squares, and can be expressed as

$$\mathbb{Y} = \mathbb{X}\boldsymbol{\beta} + \mathbf{u}, \quad (5)$$

with $\hat{\boldsymbol{\beta}} = (\mathbb{X}^\top \mathbb{X})^{-1} \mathbb{X}^\top \mathbb{Y}$. The assumption $\mathbf{u}_t \sim \mathcal{N}(0, \sigma^2 \mathbb{I}_d)$ can be relaxed by reformulating (5) as a generalized least-squares problem (see, for instance, Appendix B in [Knight et al. \(2020\)](#)). The consistency of the GNAR parameters is established by [Leeming \(2019\)](#); [Knight et al. \(2020\)](#), who derive results based on the estimated generalized least squares estimator and the results in Section 5.2 of [Lütkepohl \(2005\)](#).

2.2 Graphical models for GNAR processes

GNAR models account for potential dependencies between nodes that are not directly connected by an edge. Building on [Dahlhaus \(2000\)](#), who extended graphical models to multivariate time series, [Nason et al. \(2025\)](#) further adapted these concepts to the GNAR framework by incorporating r -stage adjacency relationships.

[Dahlhaus \(2000\)](#) introduced the concept of a partial correlation graph $G = (K, E)$ underpinning a network process, for which loosely put, the absence of an edge between two nodes is equated to the conditional independence between their respective time series (modulo process information across all other nodes), and equivalently, a corresponding zero entry in the inverse $d \times d$ -dimensional spectral density matrix.

Now recall that GNAR models introduce higher-order node–node interactions by allowing r -stage neighborhood regressions for $r \in \{1, \dots, r^*\}$, where $r^* = \max\{s_1, \dots, s_p\}$ is the maximum (active) r -stage depth derived from the GNAR model order. These interactions capture the gradual weakening of dependence between nodes as they become more distantly separated in the graph, and the influence of an r -stage neighborhood regression term diminishes as r increases and ultimately becomes negligible when $r > r^*$. Intuitively, the cross-dependence between the time series of two nodes across all lags is expected to be strongest for first-stage neighbors and weaker for nodes that are further apart. As a result, if two nodes do not belong to each other’s neighborhood, their corresponding time series are expected to have minimal influence on each other.

Theorem 2 in [Nason et al. \(2025\)](#), reproduced below, establishes a formal connection between r -stage neighborhood regression and the inverse spectral matrix, and extends to the GNAR setup the [Dahlhaus \(2000\)](#) framework that connects node pair conditional independence to the existence of a corresponding edge in the graph adjacency matrix, to now include membership in the r -stage adjacency sets.

Theorem 2.2 ([Nason et al. \(2025\)](#)). *Let $\{\mathbf{X}_t\}$ be a stationary $\text{GNAR}(p, [s_1, \dots, s_p])$ process with a static network structure $G = (K, E)$, a full-rank spectral matrix $\mathbf{f}(\omega)$, and a maximum active r -stage depth r^* . Then, the inverse spectral matrix \mathbf{S} and the node-wise distances $\delta(i, j)$ computed on the network G satisfy*

a) There exists a partial correlation graph $\tilde{G} = (K, \tilde{E})$ with the same set of nodes as G such that

$$(i, j) \notin \tilde{E} \iff \delta(i, j) \geq 2r^* + 1.$$

b) There exists a cross-spectral hierarchy $\xi^{(1)} > \dots > \xi^{(r^*)} > \xi^{(r^*+1)} = 0$ and an active r -stage neighborhood regression such that

$$\delta(i, j) \in \{2r - 1, 2r\} \iff \xi^{(r)} \leq |[\mathbf{S}(\omega)]_{ij}| < \xi^{(r-1)},$$

for all frequencies $\omega \in (0, 0.5]$ and for all stages $r \in \{1, \dots, r^*\}$.

Part (a) of Theorem 2.2 states that two time series $\{X_{i,t}\}_t$ and $\{X_{j,t+h}\}_t$ are uncorrelated at all lags h , given all other nodes, if and only if nodes i and j do not share any common active r^* -stage neighbours. In contrast to traditional graphical models for time series, the absence of an edge between two nodes in G now implies that whenever their network distance exceeds $(2r^* + 1)$, the corresponding time series $\{X_{i,t}\}$ and $\{X_{j,t+h}\}$ remain uncorrelated at all lags, conditional on all other nodal time series.

Part (b) of Theorem 2.2 establishes a link between the higher-order autocorrelation structure induced by a GNAR process and its hierarchical dependence structure, which can be identified through the inverse spectral matrix. Specifically, r -stage neighbours in G are connected by path of length $\delta(i, j) \in \{2r - 1, 2r\}$.

3 Spectral inference for stationary network time series

In this section, we introduce the GNAR spectrum in Section 3.1 and propose both parametric and nonparametric avenues for its estimation in Section 3.2. Section 3.2.1 discusses the consistency of the parametric GNAR spectrum estimator, while the construction and properties of the novel nonparametric estimation approach incorporating a penalty based on the underlying network structure are discussed in Section 3.2.2.

3.1 GNAR model spectrum

By leveraging the connection between GNAR models and constrained VAR representations discussed in Section 2.1, the GNAR spectral density can be naturally defined by embedding the network structure directly into a d -dimensional $\text{VAR}(p)$ process coefficient representation using equation (4) (see also page 685 of [Priestley, 1981](#)), as follows.

Definition 1 (GNAR Spectrum). Let $\{\mathbf{X}_t\}$ be a stationary $\text{GNAR}(p, [s_1, \dots, s_p])$ process defined on a static network $G = (K, E)$. We define the GNAR spectral density as the $d \times d$ complex-valued matrix

$$\mathbf{f}_{\text{GNAR}}(\omega) = \mathbf{U}_p^{-1}(\omega) \mathbf{V}_d \left(\overline{\mathbf{U}}_p^{-1}(\omega) \right)^\top, \quad (6)$$

where the GNAR notation in equation (2) holds with a general covariance matrix \mathbf{V}_d for the innovation

process $\{\mathbf{u}_t\}$, \cdot denotes the complex-valued conjugate, and the components $\mathbf{U}_p(\omega)$ are defined as

$$\mathbf{U}_p(\omega) = \mathbb{I}_d - \sum_{k=1}^p \left[\alpha_k \mathbb{I}_d + \sum_{r=1}^{s_k} \beta_{kr} (\mathbf{W} \odot \mathbf{A}_r) \right] e^{-i2\pi k\omega}, \quad (7)$$

for any frequency $\omega \in (0, 0.5]$.

Definition 1 extends the classical VAR spectral representation by incorporating network dependencies through the edge-weight matrix \mathbf{W} and the r -stage adjacency matrices \mathbf{A}_r , thereby effectively capturing the structural influence of the graph on the spectral properties of the process. Moreover, based on the definition of the GNAR spectrum in Definition 1, the population versions of squared coherence and squared partial coherence can be defined in Equations (8) and (9). The latter relies on the inverse of the GNAR spectrum, $\mathbf{S}_{\text{GNAR}}(\omega) := \mathbf{f}_{\text{GNAR}}(\omega)^{-1}$.

$$[\rho_{\text{GNAR}}(\omega)]_{ij}^2 = \frac{|[\mathbf{f}_{\text{GNAR}}(\omega)]_{ij}|^2}{[\mathbf{f}_{\text{GNAR}}(\omega)]_{ii} \cdot [\mathbf{f}_{\text{GNAR}}(\omega)]_{jj}}, \quad i, j = 1, \dots, d, \quad (8)$$

$$[\gamma_{\text{GNAR}}(\omega)]_{ij}^2 = \frac{|[\mathbf{S}_{\text{GNAR}}(\omega)]_{ij}|^2}{[\mathbf{S}_{\text{GNAR}}(\omega)]_{ii} \cdot [\mathbf{S}_{\text{GNAR}}(\omega)]_{jj}}, \quad i, j = 1, \dots, d. \quad (9)$$

3.2 GNAR spectral density estimation

Various estimators for the GNAR spectral density matrix may be proposed in order to obtain estimates of $\mathbf{f}_{\text{GNAR}}(\cdot)$. Based on Definition 1, a natural starting point is a parametric estimator, as this definition explicitly depends on the GNAR model parameters and the covariance structure of the innovation process.

3.2.1 Parametric estimation of the GNAR spectrum

The parametric estimation of the GNAR spectral density matrix $\mathbf{f}_{\text{GNAR}}(\cdot)$ is derived from its definition in (6), which explicitly depends on the GNAR model parameters and the covariance structure of the process. Given a chosen GNAR model order, the estimation procedure involves the following steps.

- (a) **GNAR model fitting:** As discussed in Section 2.1, the GNAR coefficients $\{\alpha_k\}_k$ and $\{\beta_{kr}\}_{k,r}$ can be estimated using least squares or penalized regression techniques, while incorporating the structure of the underlying network. Furthermore, methods for order selection to ensure proper model specification are explored in Section 3 of [Knight et al. \(2020\)](#); an oracle-type solution for selecting active modes in each r -stage neighbourhood regression and applying autoregressive coefficient shrinkage to reduce variance estimation and enhance model interpretability are presented in Section 4.2 of [Nason et al. \(2025\)](#).
- (b) **Residual covariance estimation:** The covariance matrix of the innovation process, \mathbf{V}_d , is estimated from the residuals of the fitted GNAR model. In Appendix B of [Knight et al. \(2020\)](#), a consistent estimator for the innovation covariance matrix in the GNAR setting is presented, which is adapted from [Lütkepohl \(2005\)](#). [Mantziou et al. \(2023\)](#) advocate a similar strategy in the GNAR-edge fitting context.

(c) **GNAR spectral matrix estimation:** The estimated parameters are substituted into the spectral representation in (6), leading to the parametric estimator:

$$\widehat{\mathbf{f}}_{\text{GNAR}}(\omega) = \widehat{\mathbf{U}}_p^{-1}(\omega) \widehat{\mathbf{V}}_d \left(\widehat{\mathbf{U}}_p^{-1}(\omega) \right)^\top, \quad (10)$$

where $\widehat{\mathbf{U}}_p(\omega)$ follows from (7) using the estimated GNAR parameters.

Theoretical properties for the parametric GNAR spectrum estimator. The consistency of the parametric estimator is naturally derived from the consistency of the GNAR parameter estimates under standard regularity conditions (Leeming, 2019; Knight et al., 2020). Specifically, when the true GNAR process is correctly specified, we have for the estimator in equation (10),

$$\widehat{\mathbf{f}}_{\text{GNAR}}(\omega) \xrightarrow{p} \mathbf{f}_{\text{GNAR}}(\omega), \text{ for all frequencies } \omega \in (0, 0.5]. \quad (11)$$

In practical terms, the **R** package **GNAR** provides the implementation for the least squares estimates of the GNAR parameters, from which $\widehat{\mathbf{f}}_{\text{GNAR}}(\omega)$ can be obtained via (10). While parametric estimation is a computationally efficient and interpretable method for estimating $\mathbf{f}_{\text{GNAR}}(\omega)$, its accuracy depends on the correct specification of the GNAR model and the accuracy of the parameter estimates. To mitigate the risk of model misspecification, a nonparametric estimation approach, as often discussed in the literature, can also be considered. In Sections 3.2.2 (iii) and (iv), we introduce a possible nonparametric framework for this task, leveraging the network structure and insights from the nonparametric spectral estimation literature.

3.2.2 Nonparametric estimation of the GNAR spectrum

Since a GNAR process is inherently a multivariate time series, traditional nonparametric spectral density estimation techniques, such as periodogram-based estimators, can be obtained. Moreover, again exploiting the GNAR structure viewed as a constrained VAR, the theoretical properties of these estimators remain valid for GNAR processes. Let us first recall the construction of a nonparametric spectral estimator that does not incorporate network-specific structure, with the procedure closely following standard multivariate time-series methods and involving the primary steps described below.

(i) **Fourier raw periodogram:** Consider a stationary GNAR process $\{\mathbf{X}_t\}_{t=1}^T$ over a network with d nodes. The discrete Fourier transform of $\{\mathbf{X}_t\}$ is

$$\mathbf{J}(\omega_l) = \frac{1}{\sqrt{T}} \sum_{t=1}^T \mathbf{X}_t e^{-i2\pi t \omega_l},$$

where $\omega_l = l/T$ for $l = 0, 1, \dots, n_T = ([T/2] - 1)$ are the evaluation Fourier frequencies. The $d \times d$ periodogram matrix, which serves as a raw estimate of the spectral density, is defined as

$$\mathbf{I}_T(\omega_l) = \mathbf{J}(\omega_l) \overline{\mathbf{J}}(\omega_l)^\top, \quad (12)$$

with its asymptotic behaviour studied in depth across the classical Fourier literature, see e.g., Section 11.7 in [Brockwell and Davis \(1991\)](#). Under the assumption that the process $\{\mathbf{X}_t\}$ is Gaussian with an absolutely summable autocovariance function (to which we henceforth refer as Assumption A), it is well known that asymptotically $\mathbf{J}(\omega_l) \sim N_{\mathbb{C}}(\mathbf{0}, \mathbf{f}_{\text{GNAR}}(\omega_l))$, approximately independent at different Fourier frequencies.

(ii) **Smoothed periodogram:** To obtain a consistent estimator of the spectral matrix \mathbf{f}_{GNAR} , the periodogram needs to be smoothed. Given the bandwidth parameter $m_T = o(\sqrt{T})$ and weight function $\{W_T(\cdot)\}$, a smoothed spectral estimator $\tilde{\mathbf{I}}_T(\omega_l)$ is defined as

$$\tilde{\mathbf{I}}_T(\omega_l) = \frac{1}{2m_T + 1} \sum_{|k| \leq m_T} W_T(k) \mathbf{I}_T(\omega_{(l+k) \text{mod}(T)}). \quad (13)$$

For guidance on the bandwidth and weight choices, see [Priestley \(1981\)](#). The consistency of the smoothed periodogram is discussed in e.g., [Brockwell and Davis \(1991\)](#); [Shumway and Stoffer \(2017\)](#).

Under Assumption A and recalling that for a Gaussian time series, the Fourier coefficients are asymptotically $\mathbf{J}(\omega_l) \sim N_{\mathbb{C}}(\mathbf{0}, \mathbf{f}_{\text{GNAR}}(\omega_l))$ at every frequency ω_l and approximately independent across frequencies, an approximation to the (pseudo) log-likelihood can be constructed and used in order to estimate the spectral density and precision under e.g., further sparsity constraints ([Deb et al., 2024](#)). This approximation at ω_l (up to a constant) is,

$$\log \det \mathbf{f}_{\text{GNAR}}^{-1}(\omega_l) - \text{tr} \left(\mathbf{f}_{\text{GNAR}}^{-1}(\omega_l) \tilde{\mathbf{I}}_T(\omega_l) \right), \quad (14)$$

where tr denotes the trace operator.

(iii) **Nonparametric GNAR spectral estimator penalized by the underlying network structure:**

While the smoothed periodogram in (ii) above offers a flexible nonparametric approach to spectral estimation, it is agnostic of the underlying network topology that characterises GNAR processes. This omission presents a valuable opportunity: by integrating the *known* network structure into the estimation procedure, we can refine the spectral estimates and improve interpretability, as aligned with the graph's connectivity. The key property we exploit is that if two nodal time series are conditionally independent given the rest of the network (no edge between nodes, hence a zero entry in the network adjacency matrix \mathbf{A}_1), then the corresponding entry in the inverse spectrum should be zero (see also Section 2.2).

Classical methods ([Hastie et al., 2009](#); [Songsiri et al., 2009](#)) do formulate likelihood-based estimation under network-driven structural constraints, but they are generally designed for real-valued matrices, whereas the smoothed periodogram is complex-valued. To bridge this gap, we follow the approach of [Fiecas et al. \(2019\)](#); [Deb et al. \(2024\)](#), who reformulate complex-valued spectral estimation problems into equivalent real-valued settings, thus allowing for classical penalized estimation techniques to be adapted.

To achieve this, at each frequency ω_l we decompose the complex-valued smoothed periodogram $\tilde{\mathbf{I}}_T(\omega_l) \in \mathbb{C}^{d \times d}$ into its real and imaginary components, denoted by $\tilde{\mathbf{C}}(\omega_l) \in \mathbb{R}^{d \times d}$ and $\tilde{\mathbf{Q}}(\omega_l) \in \mathbb{R}^{d \times d}$, respectively.

Instead of using $\tilde{\mathbf{I}}_T(\omega_l)$ directly, we replace it with the following real-valued matrix

$$\tilde{\Sigma}(\omega_l) = \frac{1}{2} \begin{bmatrix} \tilde{\mathbf{C}}(\omega_l) & -\tilde{\mathbf{Q}}(\omega_l) \\ \tilde{\mathbf{Q}}(\omega_l) & \tilde{\mathbf{C}}(\omega_l) \end{bmatrix}. \quad (15)$$

This formulation guarantees that $\tilde{\Sigma}(\omega_l)$ serves as a consistent estimator of the true matrix $\Sigma(\omega_l)$, which corresponds to the target quantity in equation (15). The population analogue can be derived from the complex-valued spectral density matrix $\mathbf{f}_{\text{GNAR}}(\omega_l) = \mathbf{C}(\omega_l) - i\mathbf{Q}(\omega_l)$ (see, e.g., [Shumway and Stoffer, 2017](#)) and viewed as the covariance matrix of the transformed (real-valued) discrete Fourier coefficients, as shown in equation (20) of [Appendix A](#) that also contains the derivation of equation (15).

To introduce the network-based structural constraints, we enforce zeroes in the inverse covariance matrix $\Theta(\omega_l) = \Sigma^{-1}(\omega_l)$ by means of the adjacency matrix \mathbf{A}_1 , which encodes the direct interactions among nodes in the network $G = (K, E)$. Since $\Sigma(\omega_l) \in \mathbb{R}^{2d \times 2d}$, we define an augmented adjacency matrix

$$\tilde{\mathbf{A}}_1 = \begin{bmatrix} \mathbf{A}_1 & \mathbf{A}_1 \\ \mathbf{A}_1 & \mathbf{A}_1 \end{bmatrix}, \quad (16)$$

ensuring the structural constraints apply consistently across the real and imaginary blocks of $\Theta(\omega_l)$.

To estimate the constrained inverse, in the same vein as equation (14), we construct a penalized Gaussian log-likelihood as below, where for brevity we have dropped the specific dependence on frequency

$$\ell(\Theta) = \log \det \Theta - \text{tr}(\tilde{\Sigma} \Theta) - \sum_{\{(i,j) \mid (\tilde{\mathbf{A}}_1)_{i,j}=0\}} \lambda_{ij} \theta_{ij}, \quad (17)$$

and λ_{ij} are Lagrange multipliers penalizing non-zero entries corresponding to absent edges in the network. The first-order condition for maximization yields

$$\Theta^{-1} - \tilde{\Sigma} - \Lambda = 0,$$

with Λ the matrix of Lagrange multipliers above encoding the graph connectivity. This equation can be solved using iterative regression updates, as outlined in [Algorithm 17.1 of Hastie et al. \(2009\)](#), in order to obtain the refined precision estimator $\hat{\Theta}$, and the corresponding covariance matrix estimator $\hat{\Sigma} = \hat{\Theta}^{-1}$.

Finally, using (15), we derive the complex-valued, network-penalized nonparametric GNAR spectral estimator as

$$\hat{\mathbf{I}}(\omega_l) = \hat{\mathbf{C}}(\omega_l) - i\hat{\mathbf{Q}}(\omega_l).$$

Theoretical properties of the penalized estimator $\hat{\mathbf{I}}(\cdot)$, including consistency, are discussed in [Appendix B](#). We establish a connection with the formulation in [Section 2.3 of Fiecas et al. \(2019\)](#), where the smoothed periodogram is interpreted as a solution to an augmented covariance estimation problem. Building on this, we apply the maximum likelihood theory for covariance selection developed in [Dempster \(1972\)](#)

to derive asymptotic covariance results for the augmented covariance matrix and, consequently, for the proposed nonparametric estimator. This approach is closely related to the maximum likelihood estimation framework developed in Section 5.2.1 of [Lauritzen \(1996\)](#).

(iv) **Nonparametric GNAR spectral estimator penalized by the GNAR-induced adjacency:** As discussed by [Nason et al. \(2025\)](#) and summarized in Theorem 2.2 (Section 2.2), GNAR processes induce a distinct nodal correlation structure compared to traditional network time series approaches and the partial correlation graph introduced by [Dahlhaus \(2000\)](#). This distinction arises from the incorporation of information via intermediate nodes through the r -stage neighbourhood regression inherent in the GNAR framework, and in turn equates to the existence of a generalised partial correlation graph $\tilde{G} = (K, \tilde{E})$ such that the nodal time series $\{X_{i,t}\}$ and $\{X_{j,t}\}$ are uncorrelated at all lags conditional on the remaining nodes if and only if their corresponding distance in the GNAR-induced graph \tilde{G} fulfills $\delta_{\tilde{G}}(i, j) > r^*$ ([Nason et al., 2025](#), see Definition 7 in the supplement). Equivalently, this means that two nodes become uncorrelated only when their distance in the underlying network G exceeds $2r^*$, where we remind the reader that r^* is the maximum r -stage depth determined by the GNAR model order.

This structural insight suggests an alternative penalty for the smoothed spectral estimator to the proposal in (iii) above. Rather than penalizing the nonparametric estimator using the adjacency matrix \mathbf{A}_1 of the original network, we propose to instead penalize it using an adjacency matrix derived from the GNAR partial correlation graph. This GNAR-induced adjacency matrix can be defined as

$$\mathbf{A}_{\tilde{G}} = \sum_{r=1}^{\min\{2r^*, r_{\max}\}} \mathbf{A}_r,$$

where each \mathbf{A}_r encodes the r -stage neighbourhood connections and r_{\max} denotes the network diameter, i.e., the longest shortest-path distance between any two nodes. Its mapping from complex- to real-valued $\tilde{\mathbf{A}}_{\tilde{G}}$ can be carried out analogously to \mathbf{A}_1 in equation (16), and the penalised spectral estimator will be the solution to a problem akin to (17) with $\tilde{\mathbf{A}}_{\tilde{G}}$ replacing $\tilde{\mathbf{A}}_1$.

An important distinction emerges from this approach: unlike direct penalization by \mathbf{A}_1 , the use of $\mathbf{A}_{\tilde{G}}$ captures higher-order dependencies through the r -stage regression. Specifically, two nodal time series must be separated by more than $2r^*$ steps in the network to be conditionally uncorrelated, as intermediate nodes mediate dependencies. This agrees with Corollary 2 of the supplement in [Nason et al. \(2025\)](#), as for $r^* = 1$, the matrix $\mathbf{A}_{\tilde{G}}$ is simply the sum of the 1-stage and 2-stage adjacency matrices of the original network.

While this approach may inherit the precise correlation structure induced by the GNAR process, it comes at a cost: the sparsity of the GNAR-induced adjacency matrix $\mathbf{A}_{\tilde{G}}$ tends to decrease as the neighborhood level $r \in \{1, \dots, r^*\}$ increases. This reduction in sparsity has two potential consequences. First, the estimation of the GNAR spectral density may become more challenging due to the introduction of additional parameters in the r -stage neighborhood regression, arising from the denser structure of $\mathbf{A}_{\tilde{G}}$. Second, if the maximum r -stage depth r^* exceeds the diameter of the network (r_{\max}), the penalization may

no longer provide meaningful structural constraints, as the network effectively becomes fully connected. We investigate the practical implications of this penalization strategy in Section 4.

3.3 GNAR spectrum r -dependent refinement

3.3.1 GNAR spectral hierarchy

In light of part (b) of Theorem 2.2 (Nason et al., 2025, also see the proof of Theorem 2 in their supplement), GNAR processes admit a conditional cross-spectral hierarchy that enables a structured representation of nodal dependence across varying network distances, as assimilated by their corresponding r -stages. This hierarchy is captured by a decreasing sequence of positive threshold parameters $\{\xi^{(r)}\}_{r=1}^{r^*}$, where each r corresponds to an r -stage neighborhood in the network, and therefore to a distance in the graph. The thresholds are connected to a family of r -dependent inverse spectral matrices, denoted by $\{\mathbf{S}^{(r)}(\cdot)\}_{r=1}^{r^*}$, which encapsulates the strength of conditional cross-spectral dependencies as a function of nodal distance.

Nason et al. (2025) propose the hierarchy construction by the entry-wise application of a complex-valued soft-thresholding operator to the inverse spectral matrix (precision), $\mathbf{S}_{\text{GNAR}}(\cdot) := \mathbf{f}_{\text{GNAR}}^{-1}(\cdot)$, thus preserving the phase of non-zero entries while setting the magnitude of small coefficients below a chosen threshold (ρ) to zero,

$$\text{sft}(z; \rho) := (|z| - \rho)_+ e^{i \arg(z)}, \text{ where } (x)_+ := \max(x, 0). \quad (18)$$

The thresholded inverse spectrum at stage r and frequency ω is then defined as

$$\mathbf{S}^{(r)}(\omega) := \left[\text{sft} \left([\mathbf{S}_{\text{GNAR}}(\omega)]_{ij} + \xi^{(r)} \cdot \mathbf{1}_{\{i=j\}} \cdot e^{i \arg([\mathbf{S}(\omega)]_{ii}); \xi^{(r)}} \right) \right]_{i,j=1}^d, \forall \omega \in (0, 0.5],$$

and ensures that as r decreases, the matrices become sparser, reflecting a model in which fewer nodes influence each other—that is, they no longer share common active r -stage neighbors. Hence as desired, the resulting sequence of matrices $\{\mathbf{S}^{(r)}(\omega)\}_r$ makes explicit the varying degrees of cross-nodal dependence.

The r -dependent GNAR spectrum at frequency ω can then also be defined as

$$\mathbf{f}^{(r)}(\omega) := \left[\mathbf{S}^{(r)}(\omega) \right]^{-1}.$$

This framework respects the GNAR model's correlation structure while providing increasingly refined approximations to the underlying spectral dependence structure through localized regularization.

3.3.2 Estimation of the r -dependent GNAR hierarchy

To estimate the r -dependent spectrum defined in Section 3.3.1, it is necessary to first determine suitable thresholds $\widehat{\xi}^{(r)}$ before applying the complex soft-thresholding operator to the estimated inverse spectrum $\widehat{\mathbf{S}}_{\text{GNAR}}(\cdot)$, e.g. following the strategy in (iii) or (iv) of Section 3.2.2. These thresholds then enable the construction of the r -dependent GNAR spectral estimators $\widehat{\mathbf{S}}^{(r)}(\cdot)$ and $\widehat{\mathbf{f}}^{(r)}(\cdot)$ for all $r = 1, \dots, r^*$. Consistency of the precision estimator for its true counterpart, \mathbf{S}_{GNAR} , directly follows from the continuous mapping

theorem (Billingsley, 1999) using the (consistent) GNAR spectral estimator, $\hat{\mathbf{f}}_{\text{GNAR}}$.

In Algorithm 1, we propose a practical approach to select the thresholds $\hat{\xi}^{(r)}$, and thereby obtaining an estimate of the r -dependent spectra.

Algorithm 1 Selection of the r -dependent spectra for a known order GNAR process

- 1: **Frequency Grid:** Choose a fine grid of evaluation frequencies $\omega \in [0, 0.5]$, as in Section 3.2.2 (i).
- 2: **Inverse Spectral Matrix:** Estimate $\hat{\mathbf{S}}_{\text{GNAR}}(\omega) = [\hat{\mathbf{f}}_{\text{GNAR}}(\omega)]^{-1} \in \mathbb{C}^{d \times d}$, $\forall \omega$, as in Section 3.2.
- 3: **Threshold Selection by Graph Distance:** For each $r = 1, \dots, r^*$, define the set $\{\varphi^{(r)}(\cdot)\}_r$ as the magnitudes of the estimated inverse spectral matrix for nodal pairs (i, j) whose network distance $\delta(i, j) \in \{2r - 1, 2r\}$, i.e.,

$$\varphi^{(r)}(\omega) := \left\{ |\hat{\mathbf{S}}_{\text{GNAR}}(\omega)_{ij}| : \delta(i, j) \in \{2r - 1, 2r\} \right\}, \forall \omega.$$

Then, for each r , set the threshold as

$$\hat{\xi}^{(r)} := \min_{\omega} \left\{ \varphi^{(r)}(\omega) \right\}.$$

- 4: **Threshold Inverse Spectrum:** For each frequency ω and stage r , define the thresholded inverse spectrum

$$\hat{\mathbf{S}}^{(r)}(\omega) := \left[\text{sft} \left([\hat{\mathbf{S}}_{\text{GNAR}}(\omega)]_{ij} + \hat{\xi}^{(r)} \cdot \mathbb{1}_{\{i=j\}} \cdot e^{i \arg([\hat{\mathbf{S}}(\omega)]_{ii})}; \hat{\xi}^{(r)} \right) \right]_{i,j=1}^d,$$

where $\text{sft}(x; \xi)$ represents a soft-thresholding operation with threshold ξ , as defined in (18).

- 5: **Estimate r -Dependent Spectra:** Construct the sequence $\{\hat{\mathbf{f}}^{(r)}(\cdot)\}_{r=1}^{r^*}$ where $\hat{\mathbf{f}}^{(r)}(\omega) := [\hat{\mathbf{S}}^{(r)}(\omega)]^{-1}$, $\forall \omega$, characterized by a decreasing sparsity in precision as r increases.

4 Simulation study

In this section, we introduce a series of simulation scenarios aimed at evaluating the estimation methods presented in Section 3. The primary objective is to assess the performance of these estimators by examining the impact of sample size T , different network structures G , and potential model misspecification.

We focus on networks with 5 and 10 nodes, generated using the **GNAR** package in **R** (see Figure 1), to evaluate the performance of seven spectral estimation approaches. These include: the Parametric GNAR spectrum (**EM1: ParGNAR**), the Parametric VAR spectrum agnostic of the network structure (**EM2: PVAR**), the Parametric VAR spectrum penalized by the induced GNAR structure (**EM3: PVAR_A**), the Parametric VAR spectrum penalized by the adjacency matrix of the underlying network (**EM4: PVAR_A1**), the Nonparametric spectrum penalized by the induced GNAR structure (**EM5: NP_A**), the Nonparametric spectrum penalized by the adjacency matrix of the underlying network (**EM6: NPA1**), and the Nonparametric spectrum that does not incorporate network information (**EM7: NP**).

Table 1 presents the true GNAR parameters and model orders for the simulation scenarios considered in Sections 4.1 and 4.2, designed to represent a variety of process behaviors, explored under Sections 4.1–4.3.

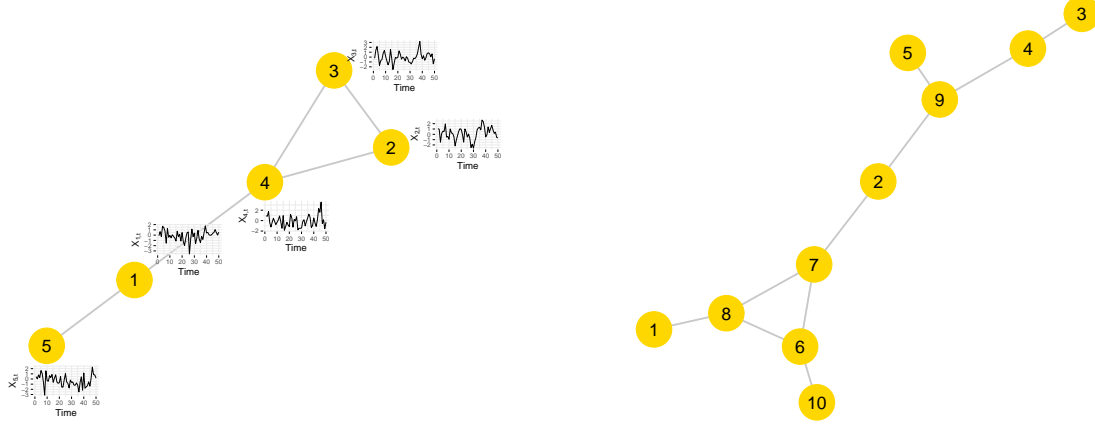


Figure 1: Networks with 5 and 10 nodes network generated with the **GNAR**  package.

Table 1: Parameter settings for GNAR simulations

Model	α_1	α_2	α_3	β
M1:GNAR(2, [1,1])	0.2	0.2	—	(0.2, 0.1) for 1-stage
M2:GNAR(2, [1,2])	0.1	0.1	—	(0.075 for 1-stage, 0.05, 0.15 for 2-stage)
M3:GNAR(2, [2,3])	0.2	0.1	—	(0.075, 0.05 for 2-stage, 0.05, 0.05, 0.1 for 3-stage)
M4:GNAR(3, [1,2,3])	0.1	0.075	0.05	(0.1 for 1-stage, 0.075 for 2-stage, 0.05 for 3-stage)
M5:GNAR(3, [3,3,3])	0.15	0.1	0.05	(0.05 for 1-stage, 0.05 for 2-stage, 0.05 for 3-stage)

4.1 Simulation under no model misspecification

In this section, the **ParGNAR** method assumes that the GNAR model order—specifically, the lag and neighborhood orders—are known as detailed in Table 1. This assumption removes any model misspecification error related to the GNAR coefficients required for estimating the parametric GNAR spectrum, as well as the coherence and partial coherence.

In order to explore spectral dependencies in the data both across the nodes and to dynamically accounting for the time dimension, we also estimate the squared coherence and squared partial coherence (defined before in equations (8) and (9), respectively) and for simplicity, we will refer to them as coherence and partial coherence from now on. Theoretically, these estimators have desirable theoretical properties, with consistency following directly from Slutsky’s theorem (Slutsky, 1925) used for the GNAR spectral estimator and its inverse. The squared coherence and partial coherence are defined for each pairs of nodes (i, j) and frequency ω as follows, with the partial coherence being computed efficiently using the approach described in Fiecas and Ombao (2011); Ombao and Pinto (2024),

Tables 2 and 3 present the root mean square error (RMSE), as defined in equation (19) using the Frobenius norm, for the seven estimation methods applied to coherence and partial coherence, respectively. The corresponding RMSE values for the estimated spectrum are provided in Table C.1 in Appendix C.

$$\text{RMSE} = \left(\frac{1}{R \cdot n_T} \sum_{rep=1}^R \sum_{\ell=1}^{n_T} \left\| \widehat{\mathbf{f}}_{\text{GNAR}}^{(rep)}(\omega_\ell) - \mathbf{f}_{\text{GNAR}}(\omega_\ell) \right\|^2 \right)^{1/2}. \quad (19)$$

The results are based on $R = 500$ independent realizations from each model, with time series lengths varying across $T = 100, 200, 500, 1000$. The parametric estimator consistently outperforms the nonparametric approaches, including the penalized network-based paradigms, and penalization under larger, sparser networks further improve the results. We note that the estimation methods penalized by the underlying network's adjacency matrix outperform those penalized by the adjacency matrix induced by the GNAR correlation structure. However, for the five-node network whose diameter is thus exceeded for the models where $r^* = 3$, the use of penalization unsurprisingly does not improve the estimation quality, i.e. for the parametric VAR and nonparametric methods. From the coherence and partial coherence results (Tables 2 and 3), it is easier to observe the superior behaviour of the parametric GNAR estimation compared to the other alternatives. As T increases, the quality of the partial coherence estimates from parametric approaches becomes similar. On the other hand, while the estimation performance improves as the sample size T increases, for low sample sizes there is a significant benefit to using the GNAR parametric estimation method, irrespective of the model complexity.

Table 2: RMSE $\times 100$ for the coherence estimates obtained using seven estimation methods (EM1–EM7) across five models (M1–M5). Results are presented for both five-node and ten-node networks under increasing time series lengths $T = 100, 200, 500, 1000$.

Model	T = 100							T = 200						
	EM1	EM2	EM3	EM4	EM5	EM6	EM7	EM1	EM2	EM3	EM4	EM5	EM6	EM7
<i>Five Nodes Network</i>														
M1	0.97	5.82	5.27	4.29	8.25	6.56	9.17	0.73	3.19	2.95	2.51	6.03	4.91	6.63
M2	1.11	5.74	5.74	4.27	8.70	6.19	8.70	0.79	3.21	3.21	2.80	6.39	4.69	6.39
M3	1.26	5.54	5.54	5.54	8.63	8.63	8.63	0.88	3.04	3.04	3.04	6.25	6.25	6.25
M4	1.48	8.22	8.22	8.22	8.73	8.73	8.73	1.05	4.43	4.43	4.43	6.40	6.40	6.40
M5	1.81	8.32	8.32	8.32	8.93	8.93	8.93	1.19	4.32	4.32	4.32	6.49	6.49	6.49
<i>Ten Nodes Network</i>														
M1	0.50	7.13	5.04	3.65	6.00	5.00	6.60	0.40	2.70	2.50	2.10	4.20	3.60	4.90
M2	0.60	6.90	5.50	3.60	6.80	5.10	6.80	0.45	2.75	2.75	2.30	4.40	3.55	4.60
M3	0.70	6.60	6.00	5.50	6.60	6.00	6.60	0.55	2.60	2.60	2.60	4.20	4.20	4.40
M4	0.85	8.40	8.00	7.50	6.90	6.50	6.90	0.70	3.80	3.80	3.80	4.50	4.20	4.40
M5	1.00	8.50	8.20	8.10	7.10	6.80	7.00	0.85	3.60	3.60	3.60	4.60	4.30	4.30
Model	T = 500							T = 1000						
	EM1	EM2	EM3	EM4	EM5	EM6	EM7	EM1	EM2	EM3	EM4	EM5	EM6	EM7
<i>Five Nodes Network</i>														

(continued on next page)

Model	T = 100							T = 200						
	EM1	EM2	EM3	EM4	EM5	EM6	EM7	EM1	EM2	EM3	EM4	EM5	EM6	EM7
M1	0.47	1.59	1.51	1.35	3.98	3.28	4.36	0.34	1.02	0.98	0.92	2.91	2.46	3.15
M2	0.53	1.62	1.62	2.08	4.24	3.40	4.24	0.35	1.01	1.01	1.89	3.08	2.75	3.08
M3	0.55	1.52	1.52	1.52	4.16	4.16	4.16	0.40	0.95	0.95	0.95	3.35	3.25	3.60
M4	0.65	1.80	1.80	1.80	4.50	4.20	4.50	0.45	1.05	1.05	1.05	3.55	3.40	3.60
M5	0.70	1.85	1.85	2.00	4.80	4.50	4.70	0.50	1.10	1.10	1.10	3.75	3.55	3.80

Ten Nodes Network

Model	T = 100							T = 200						
	EM1	EM2	EM3	EM4	EM5	EM6	EM7	EM1	EM2	EM3	EM4	EM5	EM6	EM7
M1	0.38	1.58	1.30	1.20	3.45	3.00	3.30	0.30	1.05	0.95	0.85	2.85	2.50	3.00
M2	0.45	1.72	1.55	1.40	3.80	3.10	3.80	0.35	1.15	1.05	0.95	3.10	2.60	3.20
M3	0.50	1.80	1.70	1.60	3.90	3.50	3.90	0.40	1.20	1.10	1.05	3.25	2.80	3.40
M4	0.65	2.10	2.00	1.90	4.20	3.80	4.20	0.50	1.35	1.25	1.20	3.45	3.10	3.50
M5	0.75	2.20	2.10	2.00	4.40	4.00	4.30	0.55	1.40	1.30	1.25	3.60	3.20	3.60

Table 3: RMSE $\times 100$ for the partial coherence estimates obtained using seven estimation methods (EM1–EM7) across five models (M1–M5). Results are presented for both five-node and ten-node networks under increasing time series lengths $T = 100, 200, 500, 1000$.

Model	T = 100							T = 200						
	EM1	EM2	EM3	EM4	EM5	EM6	EM7	EM1	EM2	EM3	EM4	EM5	EM6	EM7
<i>Five Nodes Network</i>														
M1	0.80	5.16	4.56	3.76	8.00	5.96	10.21	0.58	2.85	2.58	2.19	5.80	4.45	7.08
M2	0.94	5.08	5.08	4.04	9.85	6.01	9.85	0.66	2.86	2.86	2.68	6.90	4.55	6.90
M3	0.98	4.95	4.95	4.95	9.88	9.88	9.88	0.67	2.70	2.70	2.70	6.78	6.78	6.78
M4	1.15	7.30	7.30	7.30	9.81	9.81	9.81	0.81	3.92	3.92	3.92	6.81	6.81	6.81
M5	1.43	7.39	7.39	7.39	9.90	9.90	9.90	0.90	3.85	3.85	3.85	6.80	6.80	6.80

Ten Nodes Network

Model	T = 100							T = 200						
	EM1	EM2	EM3	EM4	EM5	EM6	EM7	EM1	EM2	EM3	EM4	EM5	EM6	EM7
M1	0.43	5.52	3.94	2.99	6.21	4.05	14.97	0.32	2.95	2.21	1.73	4.54	3.08	9.25
M2	0.39	5.47	4.88	2.91	9.91	3.90	14.90	0.25	2.84	2.58	1.61	6.69	2.90	9.08
M3	0.42	5.46	5.46	2.96	14.92	3.94	14.92	0.28	2.82	2.82	1.56	9.02	2.89	9.02
M4	0.47	8.28	8.28	4.15	14.85	3.89	14.85	0.34	4.21	4.21	2.20	9.09	2.94	9.09
M5	0.54	8.32	8.32	4.23	14.85	3.94	14.85	0.35	4.16	4.16	2.20	9.09	2.96	9.09

Model	T = 500							T = 1000						
	EM1	EM2	EM3	EM4	EM5	EM6	EM7	EM1	EM2	EM3	EM4	EM5	EM6	EM7

Five Nodes Network

Model	T = 500							T = 1000						
	EM1	EM2	EM3	EM4	EM5	EM6	EM7	EM1	EM2	EM3	EM4	EM5	EM6	EM7
M1	0.37	1.42	1.32	1.17	3.78	3.00	4.43	0.27	0.91	0.87	0.81	2.78	2.26	3.16
M2	0.44	1.45	1.45	1.99	4.39	3.30	4.39	0.30	0.91	0.91	1.79	3.11	2.65	3.11

(continued on next page)

Model	T = 100							T = 200						
	EM1	EM2	EM3	EM4	EM5	EM6	EM7	EM1	EM2	EM3	EM4	EM5	EM6	EM7
M3	0.42	1.31	1.31	1.31	4.26	4.26	4.26	0.29	0.79	0.79	0.79	3.10	2.67	3.10
M4	0.47	2.31	2.31	1.99	4.40	3.90	4.40	0.33	1.12	1.12	1.16	3.63	3.25	3.63
M5	0.54	2.48	2.48	2.02	4.55	3.98	4.55	0.34	1.23	1.23	1.17	3.77	3.35	3.77

Ten Nodes Network

M1	0.44	1.39	1.35	1.17	4.01	3.24	5.01	0.31	0.98	0.94	0.83	2.91	2.44	3.49
M2	0.48	1.44	1.43	1.22	4.52	3.38	5.05	0.34	0.99	0.98	0.90	3.17	2.53	3.50
M3	0.47	1.43	1.43	1.18	4.58	3.46	5.07	0.32	0.97	0.97	0.90	3.25	2.62	3.55
M4	0.50	2.30	2.30	1.89	4.72	3.86	5.18	0.36	1.11	1.11	1.02	3.67	3.12	3.85
M5	0.56	2.45	2.45	2.02	4.79	3.94	5.22	0.38	1.18	1.18	1.04	3.75	3.19	3.93

As an example, Figure 2 presents a graphical comparison of estimated and true coherence (top row) and partial coherence (bottom row) for selected node pairs in the 10-node network, using **parametric** estimation methods. The three columns correspond to the following settings: *left* — nodes 1 and 8 under Model 1; *center* — nodes 1 and 2 under Model 2; and *right* — nodes 1 and 9 under Model 4. In each case, the true coherence or partial coherence is shown as a solid red line. The selected node pairs represent increasing topological distances in the network: nodes 1 and 8 are first-stage neighbors, nodes 1 and 2 are second-stage neighbors, and nodes 1 and 9 are third-stage neighbors. Accordingly, the associated models correspond to $r^* = 1$, $r^* = 2$, and $r^* = 3$, respectively.

Across all scenarios, the parametric GNAR estimator (EM1) consistently provides the most accurate results, closely matching the true values across all frequencies. This performance is expected, given there is no model misspecification. The second-best performance is achieved by the standard VAR spectral estimator (EM2). In contrast, the penalized VAR approaches that incorporate either the network adjacency matrix or the GNAR-based adjacency structure (EM3 and EM4) perform poorly, particularly for models involving node pairs that are separated by greater topological distances. This underperformance is especially evident in the center and right panels, corresponding to Models 2 and 4, and further illustrates the appeal of using the naturally sparse structure of the GNAR estimation framework, even more so when fewer time points are available (low sample size T).

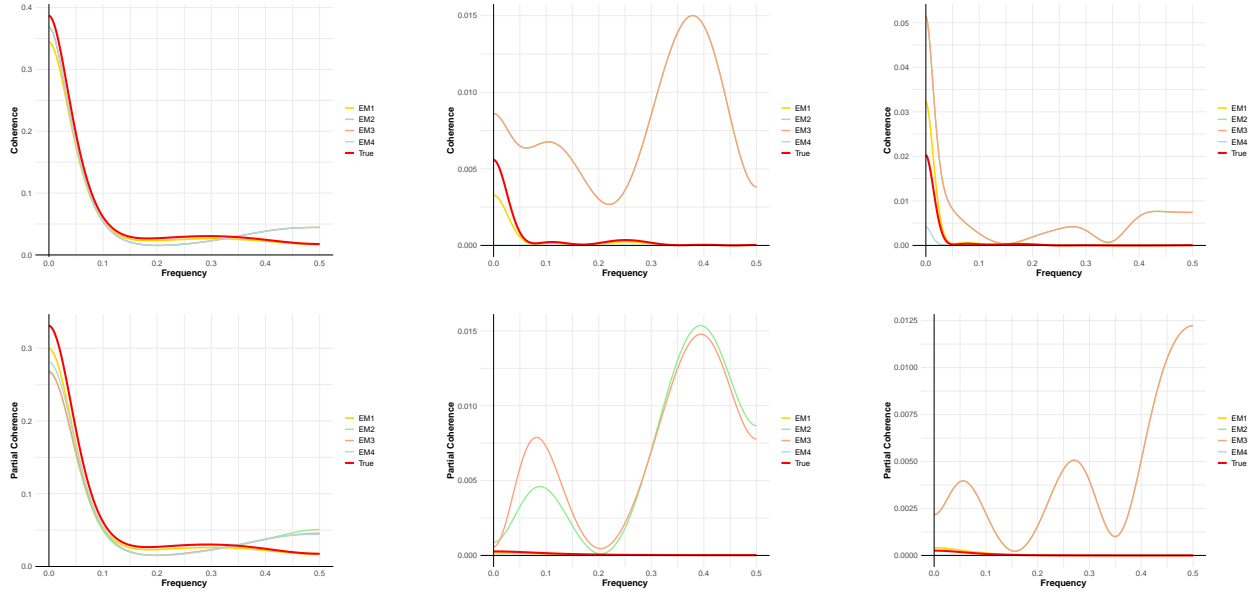


Figure 2: Graphical illustration of coherence (top row) and partial coherence (bottom row) for selected node pairs in the 10-node network using **parametric** estimation methods. The columns correspond to: *Left* – Nodes 1 and 8, *Center* – Nodes 1 and 2, *Right* – Nodes 1 and 9. Each plot compares the estimation methods to the true values.

In a similar fashion to Figure 2, Figure 3 presents a graphical comparison of estimated and true coherence (top row) and partial coherence (bottom row), now using **nonparametric** estimation methods. As anticipated, the nonparametric estimators generally perform worse than their parametric counterparts across all scenarios. Nevertheless, these results still offer valuable insights.

Among the methods, the fully nonparametric estimator that does not incorporate any network information (EM7) consistently yields the poorest performance, particularly for node pairs that are further apart in the network. In contrast, the nonparametric estimator penalized by the adjacency matrix (EM5) shows improved performance, especially in the case where the true model involves only first-stage neighbors, as seen in the left panel. Finally, the nonparametric method penalized using the GNAR-based adjacency structure (EM6) does not show substantial improvement as the network depth r increases. In fact, its performance remains poor and closely resembles that of the unpenalized estimator (EM7), particularly in the rightmost panel, where both methods produce same results.

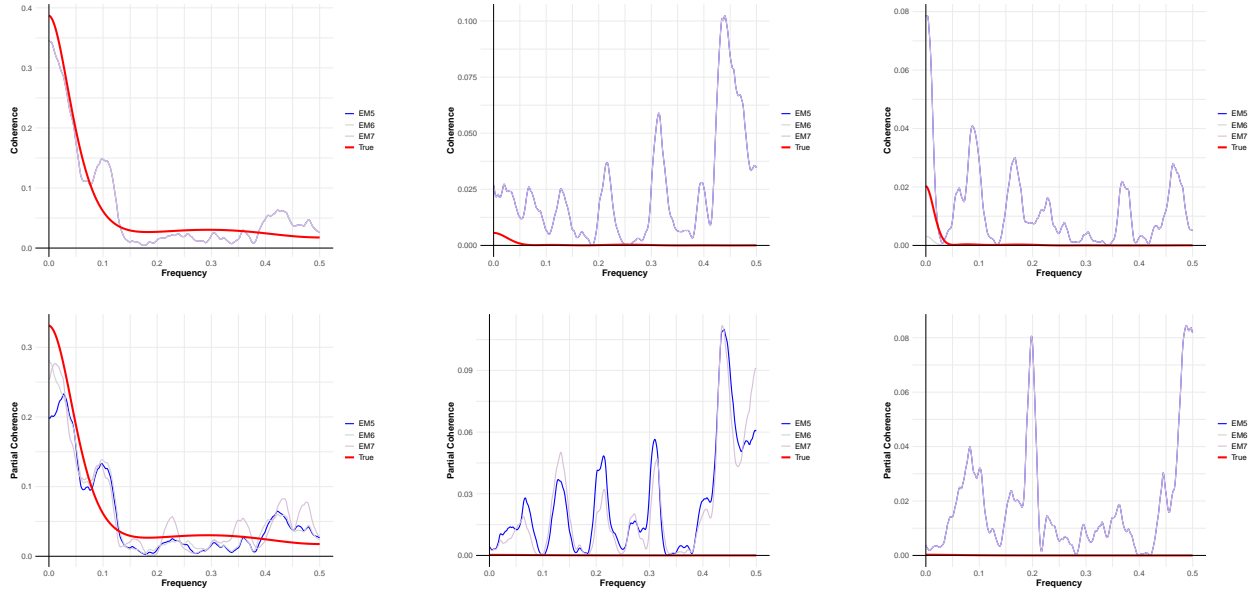


Figure 3: Graphical illustration of coherence (top row) and partial coherence (bottom row) for selected node pairs in the 10-node network using **nonparametric** estimation methods. The columns correspond to: *Left* – Nodes 1 and 8, *Center* – Nodes 1 and 2, *Right* – Nodes 1 and 9. Each plot compares the estimation methods to the true values.

4.2 Simulation under model misspecification

In this section, we examine the effects of potential model misspecification in the parametric GNAR spectrum. Specifically, the model order and the number of neighbour lags are determined using the Bayesian Information Criterion (BIC) (Schwarz, 1978), following the approach outlined in Section 3 of Knight et al. (2020). The results for the estimated spectrum, as well as for coherence and partial coherence, for the 5- and 10-node networks across $R = 500$ process replicates appear in Table 4. While there is a result depreciation due to model misspecification for low samples sizes, e.g. by a factor of 1.25×10^{-2} when $T = 100$, reassuringly the use of BIC ensures the estimator performance is maintained asymptotically with increasing sample size T .

4.3 Estimation of the r -dependent spectral representation in GNAR models

In this section, we examine the empirical performance of the r -dependent spectral representation introduced in Section 3.3.2. Specifically, we apply the parametric GNAR spectral estimation procedure outlined in Section 3.2.1 to the 10-node network illustrated in Figure 1, using values of $r^* = 1, 2, 3$ depending on the model under consideration. The estimated r -dependent spectrum, computed using Algorithm 1, is compared against its true counterpart for each model.

The root mean square errors (RMSE) of the estimated spectrum, coherence, and partial coherence are reported in Tables 5. The results show that the RMSE decreases not only as the time series length T increases, but also as the thresholds $\hat{\xi}^{(r)}$ become smaller for $r = 1, \dots, r^*$. In particular, the r -thresholded coherence and partial coherence estimates achieve noticeably lower RMSE—especially for larger r —compared

Table 4: RMSE ($\times 100$) results for GNAR across five models (M1–M5) under model misspecification, for different sample sizes $T = 100, 200, 500, 1000$.

Model	Spectrum (%)				Coherence (%)				Partial Coherence (%)			
	T=100	T=200	T=500	T=1000	T=100	T=200	T=500	T=1000	T=100	T=200	T=500	T=1000
<i>Five Nodes Network</i>												
M1	9.90	6.80	4.20	2.96	1.25	0.83	0.50	0.36	1.04	0.68	0.40	0.28
M2	8.99	5.46	3.33	2.20	1.45	0.89	0.55	0.37	1.26	0.75	0.47	0.31
M3	11.85	8.85	5.17	3.28	1.52	1.13	0.68	0.44	1.26	0.91	0.53	0.33
M4	11.61	8.93	5.96	3.81	1.71	1.30	0.88	0.55	1.37	1.02	0.66	0.41
M5	14.11	11.37	7.90	5.47	1.99	1.55	1.08	0.73	1.49	1.10	0.77	0.53
<i>Ten Nodes Network</i>												
M1	5.63	3.85	2.38	1.58	0.72	0.49	0.29	0.19	0.63	0.43	0.25	0.17
M2	4.97	2.95	1.80	1.23	0.63	0.35	0.23	0.16	0.55	0.30	0.19	0.13
M3	6.68	4.65	2.66	1.74	0.74	0.49	0.29	0.19	0.61	0.38	0.21	0.14
M4	6.12	4.72	2.88	1.76	0.73	0.56	0.34	0.22	0.59	0.43	0.26	0.16
M5	8.14	6.59	4.31	2.56	0.97	0.77	0.50	0.29	0.67	0.49	0.31	0.17

to the corresponding results in Tables 2 and 3, where no thresholding was applied. This is unsurprising, since a smaller threshold implies less modification of the precision estimator $\widehat{\mathbf{S}}(\omega)$, whereas a larger threshold isolates the effects of nodes not participating in the corresponding r -stage neighbourhood. As r increases, the reduced sparsity of the precision matrix makes the estimates less sensitive to the thresholding.

Table 5: Root mean square errors (RMSE) $\times 100$ for the estimation of the spectrum, coherence, and partial coherence using the r -dependent spectral representations. Results are shown for increasing r -stages ($r = 1, 2, 3$) and time series lengths $T = 100, 200, 500, 1000$.

Model	T = 100			T = 200			T = 500			T = 1000		
	r = 1	r = 2	r = 3	r = 1	r = 2	r = 3	r = 1	r = 2	r = 3	r = 1	r = 2	r = 3
Spectrum RMSE												
M1	4.06	—	—	3.13	—	—	2.31	—	—	1.84	—	—
M2	4.11	3.37	—	3.63	2.25	—	3.26	1.47	—	3.18	1.06	—
M3	5.05	4.29	4.56	4.69	3.18	3.23	4.56	2.11	2.00	4.74	1.72	1.47
M4	5.58	4.62	4.82	5.09	3.34	3.43	4.94	2.23	2.18	4.84	1.76	1.58
M5	6.80	6.18	6.17	6.31	5.08	4.53	6.40	4.23	3.07	6.76	3.73	2.29
Coherence RMSE												
M1	0.50	—	—	0.38	—	—	0.27	—	—	0.21	—	—
M2	0.47	0.45	—	0.43	0.29	—	0.41	0.19	—	0.41	0.14	—
M3	0.52	0.49	0.54	0.48	0.36	0.38	0.47	0.23	0.23	0.49	0.19	0.17
M4	0.66	0.57	0.61	0.63	0.43	0.44	0.63	0.28	0.28	0.64	0.23	0.20
M5	0.76	0.73	0.74	0.72	0.59	0.52	0.76	0.50	0.35	0.83	0.46	0.26
Partial Coherence RMSE												
M1	0.43	—	—	0.33	—	—	0.24	—	—	0.20	—	—

Continued on next page

Model	T = 100			T = 200			T = 500			T = 1000		
	r = 1	r = 2	r = 3	r = 1	r = 2	r = 3	r = 1	r = 2	r = 3	r = 1	r = 2	r = 3
M2	0.39	0.39	–	0.34	0.24	–	0.31	0.16	–	0.31	0.12	–
M3	0.37	0.40	0.41	0.30	0.27	0.28	0.26	0.16	0.17	0.26	0.12	0.12
M4	0.44	0.46	0.47	0.37	0.33	0.34	0.33	0.21	0.21	0.32	0.15	0.15
M5	0.42	0.50	0.52	0.31	0.33	0.34	0.25	0.20	0.20	0.23	0.15	0.14

To further assess the performance of the r -dependent estimation procedure, we examine the coherence and partial coherence functions for selected node pairs under Model 3, where the underlying 10-node network has a maximum neighborhood depth of $r^* = 3$. Figure 4 illustrates the estimated coherence (top row) and partial coherence (bottom row) for three values of $r = 1, 2, 3$, corresponding to the left, center, and right columns, respectively. The analysis focuses on three representative node pairs: nodes 1 and 8 (first-stage neighbors, shown in blue), nodes 1 and 2 (third-stage neighbors, shown in green), and nodes 1 and 4 (fifth-stage neighbors, shown in red). In each plot, the true coherence or partial coherence is displayed as a dashed line for reference.

The results highlight two key patterns. First, both coherence and partial coherence values generally decrease as the distance between nodes increases across network stages, illustrating the effectiveness with which nodal co-dependence information is being extracted as a function of r -stage, with nearly flat curves observed for the most distant pair (nodes 1 and 4). Second, increasing r (and hence reducing the threshold $\hat{\xi}^{(r)}$) improves estimation accuracy with more information being used, as the thresholded estimates more closely approximate the true functions. The resulting estimate $\hat{\mathbf{S}}^{(r)}$ is therefore less distorted by thresholding and more similar to $\hat{\mathbf{S}}$, since larger neighborhoods contribute to the estimation. These findings underscore the importance of selecting an appropriate r that adequately reflects the dependency structure of the network.

5 Application: Global bank network connectedness and its spectral features

5.1 Data and motivation

Understanding the interdependence among financial institutions is essential for assessing systemic risk and the propagation of financial contagion. A widely used approach to capture these interconnections is through *connectedness networks*, which quantify how shocks or uncertainty in one institution influence others, either directly or indirectly. This framework forms the basis of several influential studies; see, e.g., [Diebold and Yilmaz \(2009, 2014\)](#); [Demirer et al. \(2018\)](#); [Baruník and Křehlík \(2018\)](#); [Billio et al. \(2012\)](#).

[Demirer et al. \(2018\)](#), constructed a global volatility network using data from 96 publicly traded banks across 29 developed and emerging economies. The sample period runs from September 12, 2003 to February 7, 2014, and includes nearly all globally systemically important banks (GSIBs) identified by the Basel Committee, except for those not publicly listed at the beginning of the sample. Among these, 82 banks

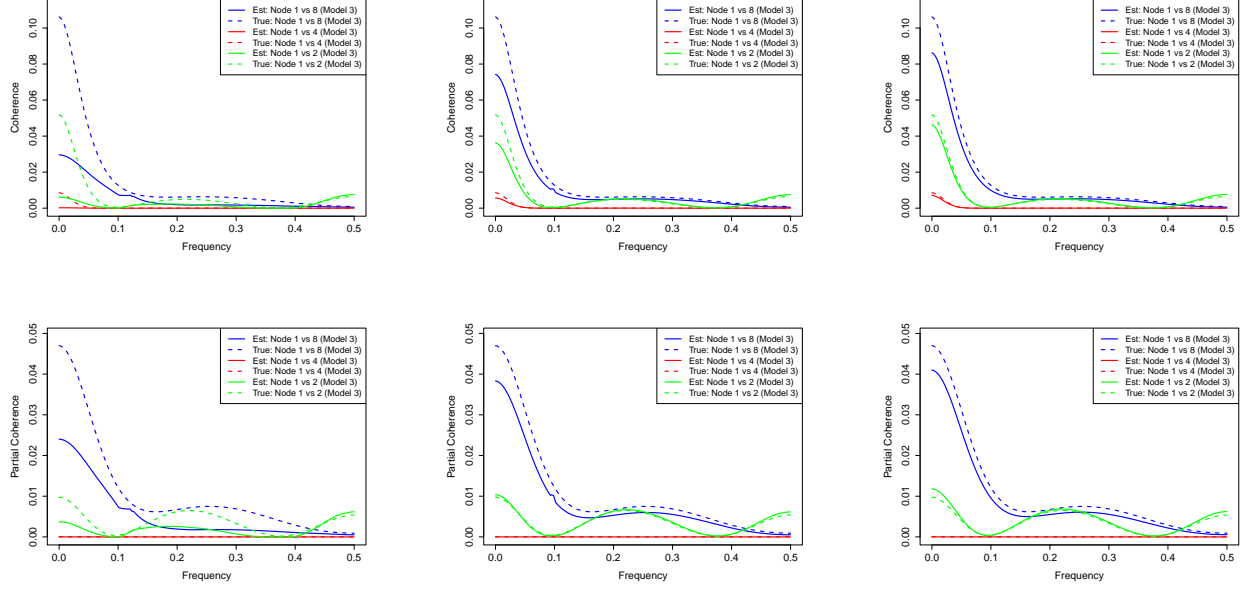


Figure 4: Comparison of estimated coherence (top row) and partial coherence (bottom row) across different levels of r . The left, center, and right columns correspond to $r = 1$, $r = 2$, and $r = 3$, respectively. For Model 3, three node pairs are selected: nodes 1 and 8 (blue), nodes 1 and 4 (red), and nodes 1 and 2 (green). In each case, the true coherence or partial coherence is shown as a dashed line.

belong to developed markets and 14 to emerging economies. The authors used daily stock return volatility as a proxy for risk. Unlike balance sheet data, market-based volatility measures are timely and directly observable, with high volatility often interpreted as a signal of market stress or investor fear. To estimate daily volatility, Demirer et al. (2018) employ the range-based Garman–Klass estimator (Garman and Klass, 1980), which has been shown to be efficient for high-frequency financial data. To be precise, the daily volatility for each bank i is computed as

$$\hat{\sigma}_{i,t}^2 = 0.511(H_{i,t} - L_{i,t})^2 - 0.019[(C_{i,t} - O_{i,t})(H_{i,t} + L_{i,t} - 2O_{i,t}) - 2(H_{i,t} - O_{i,t})(L_{i,t} - O_{i,t})] - 0.383(C_{i,t} - O_{i,t})^2,$$

where $O_{i,t}$, $H_{i,t}$, $L_{i,t}$, $C_{i,t}$ denote the open, high, low, and close prices of bank i on day t , respectively.

5.2 Data pre-processing and stationarity testing

Our framework is built upon the premise of weak stationarity, thus we perform tests for both mean and second-order stationarity. While many econometric studies rely solely on unit root tests, such as the Augmented Dickey-Fuller (ADF) test (Muñoz Mendoza et al., 2024), these tests only address mean stationarity and often overlook the second-order properties essential for weak stationarity. To overcome this limitation, we apply the locally stationary wavelet (LSW) test developed by Nason (2013), which rigorously assesses second-order stationarity by detecting time-varying dependencies in the covariance structure. When applied

to the original dataset from [Demirer et al. \(2018\)](#), some time series fail the LSW test.

As a preprocessing step, we apply a logarithmic transformation to the estimated daily volatilities. This standard procedure in financial time series analysis helps stabilize variance and normalize the scale across different assets. After the transformation, 57 of the original 96 banks pass the LSW test at the 5% significance level. The banks that pass the test are listed in Table D.2 in Appendix D, grouped by region. Our subsequent analysis focuses exclusively on this subset.

To establish the notation, the dataset we proceed to analyze is (\mathbf{X}_t, G) where $\mathbf{X}_t = \{X_{i,t}\}_{i=1}^{57}$ given by

$$X_{i,t} = \log(\hat{\sigma}_{i,t}),$$

over the graph $G = (K, E)$, with the set of nodes K encompassing the 57 banks, and the set of edges E estimated using the methodology outlined in [Demirer et al. \(2018\)](#), and described next in our context.

5.3 Network construction via GFEVD

Following [Demirer et al. \(2018\)](#), we estimate a static network of volatility spillovers among banks using the Generalized Forecast Error Variance Decomposition (GFEVD). The procedure involves three main steps: (i) sparse VAR model fitting, (ii) moving average (MA) representation, and (iii) network construction based on GFEVD.

Step (i): Sparse VAR estimation. Letting $\mathbf{X}_t \in \mathbb{R}^d$ be the vector of log-volatility series across all $d = 57$ banks at time t , we estimate a sparse VAR model of order p as

$$\mathbf{X}_t = \sum_{k=1}^p \boldsymbol{\Pi}_k \mathbf{X}_{t-k} + \boldsymbol{\varepsilon}_t.$$

To estimate the coefficients $\{\boldsymbol{\Pi}_k\}_{k=1}^p$ in the model above, we employ Lasso regression with lag order p selected by the Bayesian Information Criterion (BIC, [Schwarz \(1978\)](#)). Specifically, each equation is estimated separately using Lasso regression with 10-fold cross-validation to select the penalty parameter, and the residual covariance matrix $\hat{\mathbf{V}}$ is obtained from the fitted residuals.

Step (ii): Moving average (MA) representation. The estimated VAR coefficients are then used to obtain the MA representation

$$\mathbf{X}_t = \sum_{h=0}^{\infty} \mathbf{B}_h \boldsymbol{\varepsilon}_{t-h},$$

where $\mathbf{B}_0 = \mathbb{I}_d$, and for $h \geq 1$,

$$\mathbf{B}_h = \sum_{j=1}^{\min\{h,p\}} \mathbf{B}_{h-j} \hat{\boldsymbol{\Pi}}_j.$$

In practice, the MA coefficients are computed up to a finite forecast horizon $H = 10$.

Step (iii): GFEVD and network construction. Using the MA representation and residual covariance matrix, we compute the GFEVD as proposed by [Pesaran and Shin \(1998\)](#). For each pair of banks (i, j) , the contribution of shocks from node (bank) j to the forecast error variance of node i over horizon H is given by

$$\psi_{ij}(H) = \frac{1}{\widehat{\mathbf{V}}_{jj}} \times \frac{\sum_{h=1}^H (\mathbf{e}_i^\top \mathbf{B}_h \widehat{\mathbf{V}} \mathbf{e}_j)^2}{\sum_{h=1}^H \mathbf{e}_i^\top \mathbf{B}_h \widehat{\mathbf{V}} \mathbf{B}_h^\top \mathbf{e}_i},$$

where $\widehat{\mathbf{V}}_{jj}$ is the j -th diagonal element of $\widehat{\mathbf{V}}$, and $\mathbf{e}_i \in \mathbb{R}^d$ is a canonical basis vector selecting node i .

The resulting GFEVD matrix $\Psi(H) = [\psi_{ij}(H)]$ is row-normalized so that $\sum_j \psi_{ij}(H) = 1$ for all i . To construct an undirected network, we define edges based on a connectivity-preserving threshold τ^* . Namely, for each candidate threshold $\tau \in \mathcal{T}$, an edge is included between nodes i and j if either $\psi_{ij}(H) \geq \tau$ or $\psi_{ji}(H) \geq \tau$. The optimal threshold is selected as

$$\tau^* = \max \{ \tau \in \mathcal{T} : G(\tau) \text{ is connected} \},$$

where $G(\tau)$ denotes the graph induced by threshold τ and the desired set of edges is $E := E(\tau^*)$.

Edges in the final undirected network $G = (K, E)$ are assigned weights based on the symmetric average of bilateral contributions,

$$w_{ij} = \frac{1}{2} (\psi_{ij} + \psi_{ji}).$$

This procedure yields a symmetric, weighted adjacency matrix that captures volatility spillovers between financial institutions. The edge weights reflect the intensity of pairwise directional influences. All GFEVD quantities are computed using the `ConnectednessApproach` R package developed by [Gabauer \(2022\)](#).

Resulting empirical network. Figure 5 shows the estimated undirected network. Consistent with [Demirer et al. \(2018\)](#), the network exhibits clear clustering patterns, with banks from the same country forming tightly connected subnetworks. Banks in the Americas and Europe display strong cross-regional links, while Asian banks appear more isolated, even from others within the region. Due to the separation of Asian countries, the full layout in Figure 5 appears visually cluttered. For clarity, Figure D.1 in Appendix D provides a zoomed-in view excluding Asian countries. Finally, Figure D.2 in Appendix D depicts the r -stage neighborhood structures in the global volatility network, revealing local and multi-hop spillover patterns with dependencies extending up to five stages.

5.4 Spectral network dependence in financial time series via GNAR models

To analyze the frequency-domain dependence structure of the multivariate log-volatility series $\{\mathbf{X}_t\}_{t=1}^T$, observed across $d = 57$ financial institutions, we adopt the GNAR model ([Knight et al., 2020](#)) introduced in Section 2.1. The appeal of this framework in this data context is to capture autoregressive volatility dynamics subject to a static network structure, where dependencies are constrained by r -stage neighborhood adjacency matrices. These matrices are derived from the thresholded GFEVD-based volatility network in Figure 5.

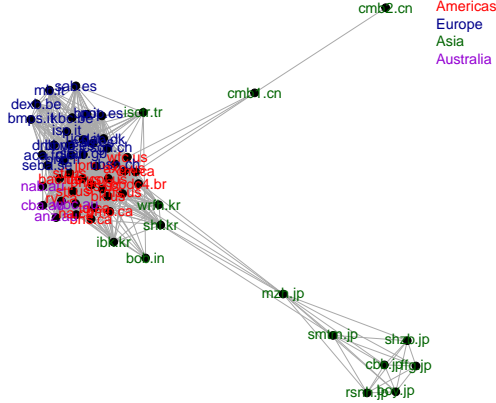


Figure 5: Undirected adjacency network estimated via GFEVD from log-volatility series using Lasso-VAR.

To determine the GNAR model order, we use the PNACF Corbit plot proposed by [Nason et al. \(2025\)](#). Figure D.3, shown in Appendix D, indicates that a GNAR(2, [1, 1]) model is appropriate.

Upon fitting the GNAR model, we compute the corresponding parametric spectral density matrix $\hat{f}_{\text{GNAR}}(\cdot)$, following the estimation procedure in Section 3.2. To examine and visualize frequency-specific interactions among institutions, we examine nine representative node pairs. These include three directly connected pairs from the same country, three directly connected pairs from different countries, and three disconnected pairs—defined as node pairs not connected by a direct (first-stage) edge. The disconnected pairs are instead linked only through multi-stage ($r > 1$) paths within the network.

Figure 6 displays several spectral summaries for these node pairs across frequencies ω : the modulus $|[\hat{\mathbf{f}}_{\text{GNAR}}(\omega)]_{ij}|$ measures the strength of frequency-domain interaction; the phase $\arg([\hat{\mathbf{f}}_{\text{GNAR}}(\omega)]_{ij})$ reveals potential lead-lag relationships; the squared coherence $[\hat{\rho}_{\text{GNAR}}(\omega)]_{ij}^2$ quantifies the total linear association at each frequency; and the squared partial coherence $[\hat{\gamma}_{\text{GNAR}}(\omega)]_{ij}^2$ isolates direct interactions conditional on all other nodes. Each curve is color-coded by connection type: red for within-country connected pairs, blue for cross-country connected pairs, and gray for disconnected pairs. As expected, the within-country connected pairs exhibit the strongest frequency-domain relationships, followed by the cross-country connected pairs. Disconnected pairs show the weakest interactions overall.

To further illustrate the behavior of disconnected nodes, Figure D.4 in Appendix D focuses exclusively on three pairs: `jpm.us-rsnh.jp`, `cmb2.cn-mb.it`, and `cmb2.cn-shzb.jp`, which correspond to 3-stage, 4-stage, and 5-stage neighbors, respectively. These results reveal a clear pattern: as the network distance r increases, both the cross-spectral magnitude and coherence decrease, confirming that longer network paths lead to weaker—but still detectable—indirect frequency-domain dependencies.

The phase behavior across frequencies offers further insight. As shown in the top right panel of Figure 6, most connected node pairs—whether within or across countries—exhibit phase values close to zero across all

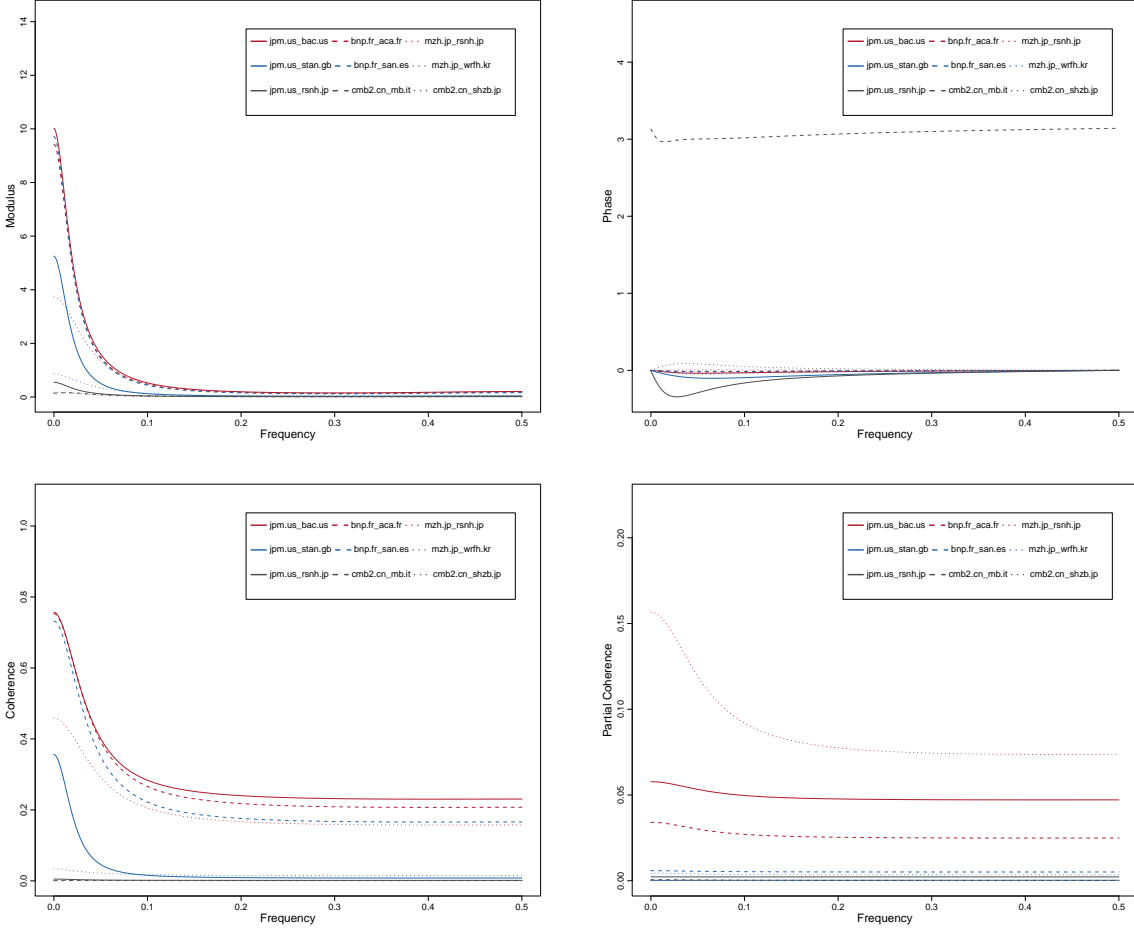


Figure 6: Spectral summaries for nine selected bank pairs (i, j) . Top row: modulus $|\hat{f}_{\text{GNAR}}(\cdot)_{ij}|$ and phase $\arg([\hat{f}_{\text{GNAR}}(\cdot)_{ij}]^2)$ of estimated cross-spectra. Bottom row: squared coherence $[\hat{\rho}_{\text{GNAR}}(\cdot)]_{ij}^2$ and partial coherence $[\hat{\gamma}_{\text{GNAR}}(\cdot)]_{ij}^2$. Colors indicate connection type: red (same-country), blue (cross-country), gray (disconnected).

frequencies. This suggests strong co-movement with little evidence of a lead-lag relationship. In contrast, the disconnected pairs (Figure D.4, top right) display noticeable variation in phase over frequencies, particularly for lower-frequency components. For the 3-stage and 4-stage neighbors, phase shifts appear at low frequencies but return toward zero as the frequency increases, implying that while long-run dynamics may exhibit directional dependence, short-term interactions are more synchronous. The 5-stage neighbor pair, however, displays a consistent phase inversion across all frequencies, indicating that the two nodes are predominantly out of phase and thus behave in an opposing manner.

These results confirm that the GNAR spectrum effectively captures both direct and indirect network-induced dependencies in the frequency domain. Moreover, the GNAR spectral estimates are broadly consistent with the findings of [Demirer et al. \(2018\)](#), while also revealing additional temporal and structural features of the volatility transmission process. In particular, GNAR spectral analysis offers novel insights into both short- and long-term interactions across financial institutions, especially in cases where nodes are

not directly connected but influence each other through multi-stage network paths.

6 Discussion

We developed a spectral estimation framework for Generalized Network Autoregressive (GNAR) processes that explicitly incorporates the network topology into the frequency-domain analysis of network time series. By including dependencies beyond immediate neighbors through r -stage neighborhoods, our approach captures more detailed signal propagation across nodes at different frequencies. We defined the GNAR spectral density and proposed both parametric and network-penalized nonparametric estimators, leveraging the model's parsimony to efficiently handle high-dimensional network time series compared to traditional VAR methods. This integration of graph topology into spectral estimation offers a flexible and interpretable tool for analyzing complex network time series data, and has wide applicability across sectors where network data is collected.

The effectiveness of our methods was studied through extensive simulations, with the parametric GNAR estimator performing strongly. The practical utility of our proposal was demonstrated in an application to global bank network connectedness, where it revealed frequency-dependent relationships and complex volatility transmission patterns consistent with existing measures. These results underscore the framework's potential to improve understanding of systemic risk by revealing how inter-bank dependencies evolve over time and across network structures in global financial systems.

Supplementary Materials

Code Reproducibility. The R code used to reproduce the simulation studies described in this paper is publicly available at the following repository: https://github.com/cfjimenezv07/GNAR_Spectral_Analysis.

Acknowledgments

The authors are grateful for the comments from participants at the second and third NeST annual meetings (London and Bath) in 2024 and 2025.

Funding

Jiménez-Varón and Knight gratefully acknowledge support from the EPSRC NeST Programme Grant EP/X002195/1.

References

Baruník, J. and T. Křehlík (2018). Measuring the frequency dynamics of financial connectedness and systemic risk. *Journal of Financial Econometrics* 16(2), 271–296.

Billingsley, P. (1999). *Convergence of Probability Measures*. Wiley.

Billio, M., M. Getmansky, A. W. Lo, and L. Pelizzon (2012). Econometric measures of connectedness and systemic risk in the finance and insurance sectors. *Journal of Financial Economics* 104(3), 535–559.

Boyd, S. and L. Vandenberghe (2004). *Convex Optimization*. Number pt. 1 in Berichte über verteilte messsysteme. Cambridge University Press.

Brillinger, D. (2001). *Time Series: Data Analysis and Theory*. Classics in Applied Mathematics. Society for Industrial and Applied Mathematics.

Brockwell, P. and R. Davis (1991). *Time Series: Theory and Methods*. Springer Series in Statistics. Springer.

Dahlhaus, R. (2000). Graphical interaction models for multivariate time series. *Metrika* 51(2), 157–172.

Deb, N., A. Kuceyeski, and S. Basu (2024). Regularized estimation of sparse spectral precision matrices. Available at: <https://arxiv.org/abs/2401.11128>.

Demirer, M., F. X. Diebold, L. Liu, and K. Yilmaz (2018). Estimating global bank network connectedness. *Journal of Applied Econometrics* 33(1), 1–15.

Dempster, A. P. (1972). Covariance selection. *Biometrics* 28(1), 157–175.

Diebold, F. X. and K. Yilmaz (2009). Measuring financial asset return and volatility spillovers, with application to global equity markets. *The Economic Journal* 119(534), 158–171.

Diebold, F. X. and K. Yilmaz (2014). On the network topology of variance decompositions: Measuring the connectedness of financial firms. *Journal of Econometrics* 182(1), 119–134.

Fiecas, M., C. Leng, W. Liu, and Y. Yu (2019). Spectral analysis of high-dimensional time series. *Electronic Journal of Statistics* 13(2), 4079 – 4101.

Fiecas, M. and H. Ombao (2011). The generalized shrinkage estimator for the analysis of functional connectivity of brain signals. *Annals of Applied Statistics* 5(2A), 1102–1125.

Friedman, J., T. Hastie, and R. Tibshirani (2007). Sparse inverse covariance estimation with the graphical lasso. *Biostatistics* 9(3), 432–441.

Gabauer, D. (2022). *ConnectednessApproach*. R package version 1.0.0.

Gabauer, D., I. Chatziantoniou, and A. Stenfors (2023). Model-free connectedness measures. *Finance Research Letters* 54, 103804.

Garman, M. B. and M. J. Klass (1980). On the estimation of security price volatilities from historical data. *Journal of Business*, 67–78.

Hastie, T., R. Tibshirani, and J. Friedman (2009). *The Elements of Statistical Learning: Data Mining, Inference, and Prediction*. Springer series in statistics. Springer.

Knight, M. I., K. Leeming, G. P. Nason, and M. A. Nunes (2020). Generalized network autoregressive processes and the GNAR package. *Journal of Statistical Software* 96, 1–36.

Lauritzen, S. (1996). *Graphical Models*. Oxford Statistical Science Series. Clarendon Press.

Leeming, K. (2019). *New Methods in Time Series Analysis: Univariate Testing and Network Autoregression Modelling*. Ph. D. thesis, University of Bristol.

Loukas, A. and N. Perraudin (2019). Stationary time-vertex signal processing. *EURASIP Journal on Advances in Signal Processing* 2019(1), 36.

Lütkepohl, H. (2005). *New Introduction to Multiple Time Series Analysis*. Springer.

Mantziou, A., M. Cucuringu, V. Meirinhos, and G. Reinert (2023). The gnar-edge model: A network autoregressive model for networks with time-varying edge weights. *arXiv preprint arXiv:2305.16097*.

Muñoz Mendoza, J. A., C. L. Veloso Ramos, C. L. Delgado Fuentealba, I. E. Araya Gómez, S. M. Sepúlveda Yelpo, and E. E. Cornejo Saavedra (2024). Connectedness in the global banking market network: Implications for risk management and financial policy. *International Review of Financial Analysis* 95, 103470.

Nason, G. (2013). A test for second-order stationarity and approximate confidence intervals for localized autocovariances for locally stationary time series. *Journal of the Royal Statistical Society Series B: Statistical Methodology* 75(5), 879–904.

Nason, G. P., D. Salnikov, and M. Cortina-Borja (2025). New tools for network time series with an application to covid-19 hospitalisations (with discussion). *J. R. Statist. Soc. A*. To appear.

Ombao, H. and M. Pinto (2024). Spectral dependence. *Econometrics and Statistics* 32, 122–159.

Pesaran, H. and Y. Shin (1998). Generalized impulse response analysis in linear multivariate models. *Economics Letters* 58(1), 17–29.

Priestley, M. B. (1981). *Spectral analysis and time series*. Academic Press Inc.

Schwarz, G. (1978). Estimating the dimension of a model. *The Annals of Statistics* 6(2), 461–464.

Shumway, R. H. and D. S. Stoffer (2017). *Time Series Analysis and Its Applications With R Examples*. Springer Texts in Statistics.

Slutsky, E. (1925). Über stochastische asymptoten und grenzwerte. *Metron* 5, 3–89.

Songsiri, J., J. Dahl, and L. Vandenberghe (2009). *Graphical models of autoregressive processes*, pp. 89–116. Cambridge: Cambridge University Press.

Wu, F., W.-L. Zhao, Q. Ji, and D. Zhang (2020). Dependency, centrality and dynamic networks for international commodity futures prices. *International Review of Economics & Finance* 67, 118–132.

A Construction of the nonparametric estimator from Section 3.2.2 (iii)

Recall we defined the smoothed periodogram matrix using a bandwidth $m_T = o(\sqrt{T})$ and kernel $W_T(\cdot)$ as

$$\tilde{\mathbf{I}}_T(\omega_l) = \frac{1}{2m_T + 1} \sum_{|k| \leq m_T} W_T(k) \mathbf{I}_T(\omega_{l+k}),$$

with the indices $l + k$ understood as evaluated modulo T . For completeness, the Fourier periodogram matrix used above is defined at frequency $\omega_l = l/T$, $l = 0, 1, \dots, n_T = ([T/2] - 1)$, as in Section 3.2.2 (i),

$$\mathbf{I}_T(\omega_l) = \mathbf{J}(\omega_l) \bar{\mathbf{J}}(\omega_l)^\top,$$

with the discrete Fourier transform (DFT) defined as

$$\mathbf{J}(\omega_l) = \frac{1}{\sqrt{T}} \sum_{t=1}^T \mathbf{X}_t e^{-i2\pi t \omega_l}.$$

We split the DFT into its real and imaginary parts as

$$\mathbf{J}(\omega_l) = \mathbf{A}(\omega_l) - i\mathbf{B}(\omega_l),$$

where

$$\mathbf{A}(\omega_l) := \text{Re}(\mathbf{J}(\omega_l)) = \frac{1}{\sqrt{T}} \sum_{t=1}^T \mathbf{X}_t \cos(2\pi t \omega_l),$$

and

$$\mathbf{B}(\omega_l) := \text{Im}(\mathbf{J}(\omega_l)) = -\frac{1}{\sqrt{T}} \sum_{t=1}^T \mathbf{X}_t \sin(2\pi t \omega_l).$$

Expressed under real-valued form, $(\mathbf{A}^\top(\omega_l), \mathbf{B}^\top(\omega_l))^\top \sim N_{2d}(\mathbf{0}, \boldsymbol{\Sigma}(\omega_l))$ (Shumway and Stoffer, 2017), where $\mathbf{f}_{GNAR}(\omega_l) = \mathbf{C}(\omega_l) - i\mathbf{Q}(\omega_l)$ and its corresponding $2d \times 2d$ covariance matrix at frequency ω_l is

$$\boldsymbol{\Sigma}(\omega_l) = \frac{1}{2} \begin{bmatrix} \mathbf{C}(\omega_l) & -\mathbf{Q}(\omega_l) \\ \mathbf{Q}(\omega_l) & \mathbf{C}(\omega_l) \end{bmatrix}. \quad (20)$$

Substituting the real and imaginary DFT parts into the periodogram and using the Hermitian transpose,

$$\mathbf{I}_T(\omega_l) = (\mathbf{A}(\omega_l) - i\mathbf{B}(\omega_l))(\mathbf{A}^\top(\omega_l) + i\mathbf{B}^\top(\omega_l)) = \mathbf{A}(\omega_l) \mathbf{A}^\top(\omega_l) + \mathbf{B}(\omega_l) \mathbf{B}^\top(\omega_l) - i(\mathbf{B}(\omega_l) \mathbf{A}^\top(\omega_l) - \mathbf{A}(\omega_l) \mathbf{B}^\top(\omega_l)).$$

Thus, the real part of the periodogram matrix is

$$\text{Re}(\mathbf{I}_T(\omega_l)) = \mathbf{A}(\omega_l)\mathbf{A}^\top(\omega_l) + \mathbf{B}(\omega_l)\mathbf{B}^\top(\omega_l),$$

and the imaginary part is

$$\text{Im}(\mathbf{I}_T(\omega_l)) = \mathbf{B}(\omega_l)\mathbf{A}^\top(\omega_l) - \mathbf{A}(\omega_l)\mathbf{B}^\top(\omega_l).$$

Finally, the smoothed periodogram matrix can be expressed as

$$\tilde{\mathbf{I}}_T(\omega_l) = \tilde{\mathbf{C}}(\omega_l) - i\tilde{\mathbf{Q}}(\omega_l),$$

where the real and imaginary parts are given respectively by

$$\tilde{\mathbf{C}}(\omega_l) = \frac{1}{2m_T + 1} \sum_{|k| \leq m_T} W_T(k) [\mathbf{A}(\omega_{l+k})\mathbf{A}^\top(\omega_{l+k}) + \mathbf{B}(\omega_{l+k})\mathbf{B}^\top(\omega_{l+k})],$$

and

$$\tilde{\mathbf{Q}}(\omega_l) = \frac{1}{2m_T + 1} \sum_{|k| \leq m_T} W_T(k) [\mathbf{B}(\omega_{l+k})\mathbf{A}^\top(\omega_{l+k}) - \mathbf{A}(\omega_{l+k})\mathbf{B}^\top(\omega_{l+k})].$$

Note that $\tilde{\mathbf{C}}(\omega_l) = \tilde{\mathbf{C}}^\top(\omega_l)$ and $\tilde{\mathbf{Q}}(\omega_l) = -\tilde{\mathbf{Q}}^\top(\omega_l)$ for any frequency ω_l . Then, in the same vein as (Shumway and Stoffer, 2017, Theorem C.6), the smoothed periodogram matrix $\tilde{\mathbf{I}}_T(\omega_l)$ can be equivalently represented in real-valued form as the symmetrical matrix

$$\tilde{\Sigma}(\omega_l) = \frac{1}{2} \begin{bmatrix} \tilde{\mathbf{C}}(\omega_l) & -\tilde{\mathbf{Q}}(\omega_l) \\ \tilde{\mathbf{Q}}(\omega_l) & \tilde{\mathbf{C}}(\omega_l) \end{bmatrix},$$

which is a well-behaved estimator for the true covariance matrix $\Sigma(\omega_l)$ defined in equation (20).

B Asymptotic properties of nonparametric estimators penalized by the network

To study the asymptotic properties of the nonparametric spectral estimator for the GNAR spectrum introduced in Section 3.2.2 (iii), we first establish some theoretical results adapted to this context, drawing in particular on Dempster (1972) and Chapter 5 of Lauritzen (1996). We establish the notation we use from here on, mainly from graphical models. Stemming from the original graph $G = (K, E)$ with d nodes and edges contained in the set E , we define a new undirected graph $\mathcal{G} = (\Gamma, \mathcal{E})$ over $2d$ nodes, where $\Gamma = \{1, \dots, 2d\}$ is the set of (new) nodes, and the new set of edges $\mathcal{E} \subseteq \Gamma \times \Gamma$ is encoded by the augmented adjacency matrix $\tilde{\mathbf{A}}_1 \in \{0, 1\}^{2d \times 2d}$ generated from the original graph G as described in equation (16).

Proposition B.1. (Adapted from Proposition 5.2 in Lauritzen, 1996) Assume that $\tilde{F}(\omega_l) \in \mathbb{R}^{2d}$ is a random vector such that $\tilde{F}(\omega_l) \sim \mathcal{N}(0, \Sigma(\omega_l))$, and let $\Theta(\omega_l) = \Sigma^{-1}(\omega_l) \in \mathbb{R}^{2d \times 2d}$ be the corresponding precision

matrix. Then the pairwise conditional independence statement

$$\tilde{F}_\gamma(\omega_l) \perp \tilde{F}_\mu(\omega_l) \mid \tilde{F}_{\Gamma \setminus (\gamma, \mu)}(\omega_l) \iff \Theta_{\gamma, \mu}(\omega_l) = 0$$

holds if and only if $(\gamma, \mu) \notin \mathcal{E}$, i.e., the absence of an edge in the graph implies conditional independence between the corresponding components of $F(\omega_l)$ given all other components.

Proof. Proposition B.1 adapts Proposition 5.2 in Lauritzen (1996), which presents the result for the multivariate normal distribution. Full details and proofs can be found therein. \square

Proposition B.2. (Adapted from Dempster, 1972; Lauritzen, 1996)

1. Let $\tilde{\Sigma}(\omega_l)$ be a well-behaved estimator of the covariance matrix $\Sigma(\omega_l)$. Then there exists a unique estimator $\hat{\Sigma}(\omega_l)$ of $\Sigma(\omega_l)$ satisfying

$$\hat{\Sigma}_{\gamma, \mu}(\omega_l) = \tilde{\Sigma}_{\gamma, \mu}(\omega_l), \quad \text{for all } (\gamma, \mu) \in \mathcal{E} \text{ or } \gamma = \mu,$$

and the constraint

$$\hat{\Theta}_{\gamma, \mu}(\omega_l) = \hat{\Sigma}_{\gamma, \mu}^{-1}(\omega_l) = 0, \quad \text{for all } (\gamma, \mu) \notin \mathcal{E}.$$

2. Among all multivariate normal models satisfying the constraint in item 1, the matrix $\hat{\Sigma}(\omega_l)$ is the maximum likelihood estimator (MLE) of $\Sigma(\omega_l)$.

Proof. 1. To see 1, we re-express the penalized log-likelihood from Section 3.2.2 (iii) over the set of edges \mathcal{E}

$$\ell(\Theta) = \log \det \Theta - \text{tr}(\tilde{\Sigma} \Theta) - \sum_{\{(\gamma, \mu) \mid (\gamma, \mu) \notin \mathcal{E}\}} \lambda_{\gamma, \mu} \theta_{\gamma, \mu}, \quad (21)$$

where $\theta_{\gamma, \mu} := \Theta_{\gamma, \mu}$ and $\lambda_{\gamma, \mu}$ are Lagrange multipliers imposing the constraint that $\theta_{\gamma, \mu} = 0$ for all $(\gamma, \mu) \notin \mathcal{E}$, and we note that we dropped the implicit frequency dependence.

Differentiating the log-likelihood in equation (21) with respect to each free parameter $\theta_{\gamma, \mu}$, we obtain the following. For diagonal entries $\gamma = \mu$, we have

$$\frac{\partial \ell}{\partial \theta_{\gamma, \gamma}} = \frac{1}{2} \frac{\partial \log \det \Theta}{\partial \theta_{\gamma, \gamma}} - \frac{1}{2} \tilde{\Sigma}_{\gamma, \gamma}, \quad (22)$$

since no penalty is imposed on the diagonal.

For off-diagonal entries $\gamma \neq \mu$, we distinguish two cases:

- If $(\gamma, \mu) \in \mathcal{E}$:

$$\frac{\partial \ell}{\partial \theta_{\gamma, \mu}} = \frac{1}{2} \frac{\partial \log \det \Theta}{\partial \theta_{\gamma, \mu}} - \tilde{\Sigma}_{\gamma, \mu}. \quad (23)$$

- If $(\gamma, \mu) \notin \mathcal{E}$:

$$\frac{\partial \ell}{\partial \theta_{\gamma, \mu}} = \frac{1}{2} \frac{\partial \log \det \Theta}{\partial \theta_{\gamma, \mu}} - \tilde{\Sigma}_{\gamma, \mu} - \lambda_{\gamma, \mu}. \quad (24)$$

Recall that the derivative of the log-determinant (see page 641 [Boyd and Vandenberghe, 2004](#)) is

$$\frac{\partial \log \det \Theta}{\partial \theta_{\gamma,\mu}} = \text{tr} \left(\Theta^{-1} \frac{\partial \Theta}{\partial \theta_{\gamma,\mu}} \right).$$

Since $\frac{\partial \Theta}{\partial \theta_{\gamma,\mu}}$ is a matrix with a 1 in the (γ, μ) and (μ, γ) positions for $\gamma \neq \mu$, and a 1 in (γ, γ) for the diagonal case, the derivative simplifies to

$$\begin{aligned} \frac{\partial \log \det \Theta}{\partial \theta_{\gamma,\gamma}} &= (\Theta^{-1})_{\gamma,\gamma}, \text{ for the diagonal,} \\ \frac{\partial \log \det \Theta}{\partial \theta_{\gamma,\mu}} &= 2(\Theta^{-1})_{\gamma,\mu}, \text{ for the off-diagonal.} \end{aligned}$$

Hence, equations (22), (23), and (24) become

For $\gamma = \mu$:

$$\frac{1}{2}(\Theta^{-1}(\omega_l))_{\gamma,\gamma} - \frac{1}{2}\tilde{\Sigma}_{\gamma,\gamma}(\omega_l) = 0, \quad \text{or} \quad (\Theta^{-1}(\omega_l))_{\gamma,\gamma} = \tilde{\Sigma}_{\gamma,\gamma}(\omega_l). \quad (25)$$

For $\gamma \neq \mu$, with $(\gamma, \mu) \in \mathcal{E}$:

$$(\Theta^{-1}(\omega_l))_{\gamma,\mu} = \tilde{\Sigma}_{\gamma,\mu}(\omega_l). \quad (26)$$

For $\gamma \neq \mu$, with $(\gamma, \mu) \notin \mathcal{E}$, the corresponding constraint forces:

$$\theta_{\gamma,\mu} = 0. \quad (27)$$

Equations (25), (26), and (27) are precisely the conditions stated in 1.

2. The specific choice of $\hat{\tilde{\Sigma}}(\omega_l)$ that satisfies the conditions in 1 corresponds to the maximum likelihood estimator $\Sigma(\omega_l)$; see, for example, [Dempster \(1972, Appendix A\)](#) and [Lauritzen \(1996, Theorem 5.3\)](#). □

By Proposition B.2, $\hat{\tilde{\Sigma}}(\omega_l)$ is the maximum likelihood estimator of $\Sigma(\omega_l)$ and under standard regularity conditions for maximum likelihood estimation, the estimator satisfies the following asymptotic properties for any Fourier frequency ω_l .

1. Consistency of the precision matrix estimator:

$$\hat{\tilde{\Theta}}(\omega_l) \xrightarrow{p} \Theta(\omega_l).$$

2. Consistency of the covariance matrix estimator:

$$\hat{\tilde{\Sigma}}(\omega_l) := \hat{\tilde{\Theta}}^{-1}(\omega_l) \xrightarrow{p} \Sigma(\omega_l).$$

Remark B.1. The results stated in Proposition B.2, which are based on the sparsity pattern induced by the adjacency matrix $\tilde{\mathbf{A}}_1$, also apply to the GNAR-induced adjacency structure introduced in Section 3.2.2 (iv). As the order r^* increases, the number of free parameters grows accordingly, and the conditions for the validity of the maximum likelihood estimator continue to hold.

C Simulation results for the estimated GNAR spectrum

Table C.1 presents the simulation results for Models (M1–M5) and estimation methods (EM1–EM7) described in Section 4.

Table C.1: RMSE $\times 100$ for the spectrum estimates obtained using seven estimation methods (EM1–EM7) across five models (M1–M5). Results are presented for both five-node and ten-node networks under increasing time series lengths $T = 100, 200, 500, 1000$.

Model	T = 100							T = 200						
	EM1	EM2	EM3	EM4	EM5	EM6	EM7	EM1	EM2	EM3	EM4	EM5	EM6	EM7
<i>Five Nodes Network</i>														
M1	7.88	32.23	31.40	27.44	30.85	27.53	31.76	5.97	21.59	21.99	19.46	26.58	23.63	27.00
M2	6.87	26.23	26.23	22.80	26.16	23.08	26.16	4.77	16.92	16.92	16.37	22.27	20.20	22.27
M3	8.91	27.39	27.39	27.39	27.11	27.11	27.11	6.27	17.77	17.77	17.77	23.23	23.23	23.23
M4	9.91	35.33	35.33	35.33	26.78	26.78	26.78	6.95	21.73	21.73	21.73	22.80	22.80	22.80
M5	12.39	37.39	37.39	37.39	28.77	28.77	28.77	8.87	22.91	22.91	22.91	24.39	24.39	24.39
<i>Ten Nodes Network</i>														
M1	3.96	41.72	34.13	28.09	24.86	20.67	29.79	2.92	24.18	20.58	17.33	21.61	17.97	25.95
M2	3.41	33.59	32.02	21.09	24.01	15.91	25.08	2.27	18.81	17.97	12.31	20.64	13.80	21.64
M3	4.66	34.17	32.66	21.21	22.36	16.58	23.36	3.11	18.83	18.03	11.38	18.81	14.68	20.20
M4	5.01	39.61	34.87	27.84	23.19	17.78	24.86	3.35	21.84	20.33	14.54	19.93	15.88	21.95
M5	6.48	41.16	36.45	28.98	24.78	19.03	27.91	4.47	22.63	20.37	16.22	20.18	17.28	22.74
Model	T = 500							T = 1000						
	EM1	EM2	EM3	EM4	EM5	EM6	EM7	EM1	EM2	EM3	EM4	EM5	EM6	EM7
<i>Five Nodes Network</i>														
M1	3.88	13.09	14.72	13.37	21.47	19.02	21.38	2.82	9.18	11.72	9.95	15.46	13.13	17.44
M2	3.11	10.17	10.17	12.46	17.90	17.15	17.90	2.10	6.94	6.94	9.59	14.22	11.57	14.22
M3	3.94	10.72	10.72	10.72	18.64	18.64	18.64	2.89	7.53	7.53	7.53	14.72	14.72	14.72
M4	4.40	12.72	12.72	12.72	18.27	18.27	18.27	3.07	8.86	8.86	8.86	14.77	14.77	14.77
M5	5.80	13.74	13.74	13.74	19.28	19.28	19.28	3.99	9.43	9.43	9.43	15.23	15.23	15.23
<i>Ten Nodes Network</i>														
M1	1.98	13.67	13.40	11.87	17.83	14.96	20.93	1.37	9.30	10.81	9.95	15.46	13.13	17.44

(continued on next page)

Model	T = 100							T = 200						
	EM1	EM2	EM3	EM4	EM5	EM6	EM7	EM1	EM2	EM3	EM4	EM5	EM6	EM7
M2	1.48	10.48	10.43	8.22	16.83	11.67	18.55	1.00	6.86	6.86	6.86	14.25	9.84	15.70
M3	1.98	10.95	10.38	8.51	15.69	12.50	16.11	1.16	7.39	7.39	6.71	13.87	10.48	13.59
M4	2.17	11.39	10.78	10.24	15.41	12.30	16.29	1.28	7.47	6.79	6.91	13.50	10.44	13.92
M5	2.68	11.90	10.84	10.35	15.86	12.44	17.22	1.54	7.93	7.22	7.38	13.99	11.06	14.71

D Supplementary visualizations and details for the global bank network connectedness application in Section 5

This appendix provides additional details about the global bank connectedness application discussed in Section 5. For example, a zoomed-in view of the network for the Americas and European countries is shown in Figure D.1, and the r -stage neighborhood structure of the network is presented in Figure D.2. The Corbit plot used for GNAR order selection, discussed in Section 5.4, is displayed in Figure D.3. Finally, further analysis of the disconnected nodes considered in Section 5.4 is provided in Figure D.4.

Table D.2: Regional Distribution of Stationary Bank Codes. Details on the corresponding bank names are provided in the Online Appendix of [Demirer et al. \(2018\)](#).

Region	Banks
Americas	jpm.us, bac.us, wfc.us, gs.us ms.us, td.ca, ry.ca, bns.ca bmo.ca, cm.ca, bk.us, bbdc4.br pnc.us, cof.us, stt.us, na.ca sti.us, fitb.us, axp.us
Europe	bnp.fr, aca.fr, gle.fr, san.es ucg.it, ubsn.ch, csgn.ch, isp.it bbva.es, stan.gb, dan.dk, kbc.be dexb.be, bmps.it, sab.es, pop.es bp.it, seba.se, dnb.no
Asia	mzh.jp, rsnh.jp, smtm.jp, wrfh.kr shf.kr, ibk.kr, ffg.jp, boy.jp cbb.jp, shzb.jp, bob.in, isctr.tr cmb1.cn, cmb2.cn
Australia	nab.au, cba.au, anz.au, wbc.au

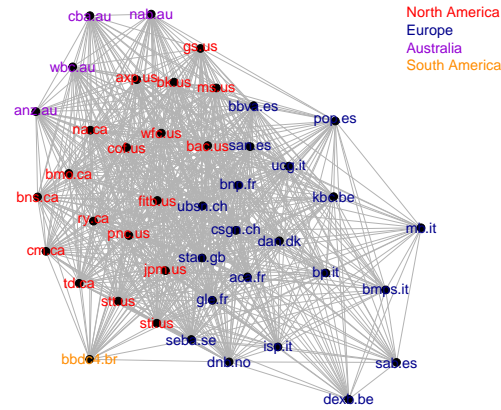


Figure D.1: Zoomed-in adjacency network excluding Asian countries, estimated via GFEVD from log-volatility series using Lasso-VAR.

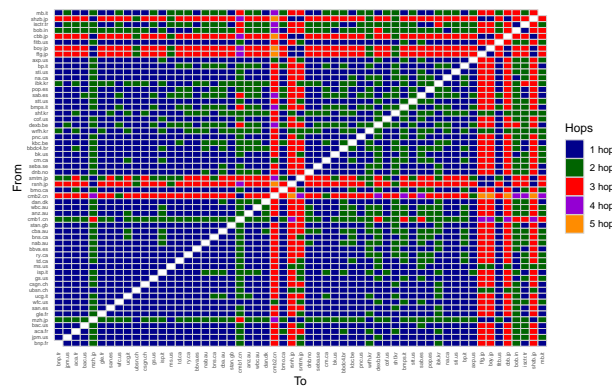


Figure D.2: r -stage neighborhood structures in the global volatility network.

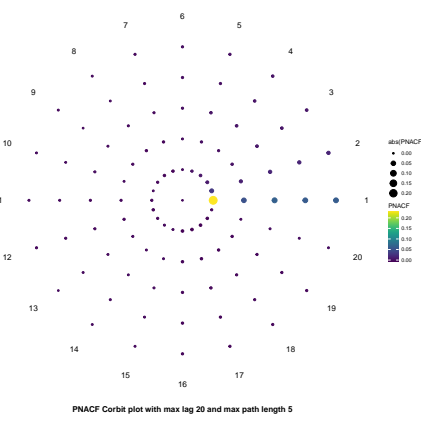


Figure D.3: PNACF Corbit plot for the log-volatility series.

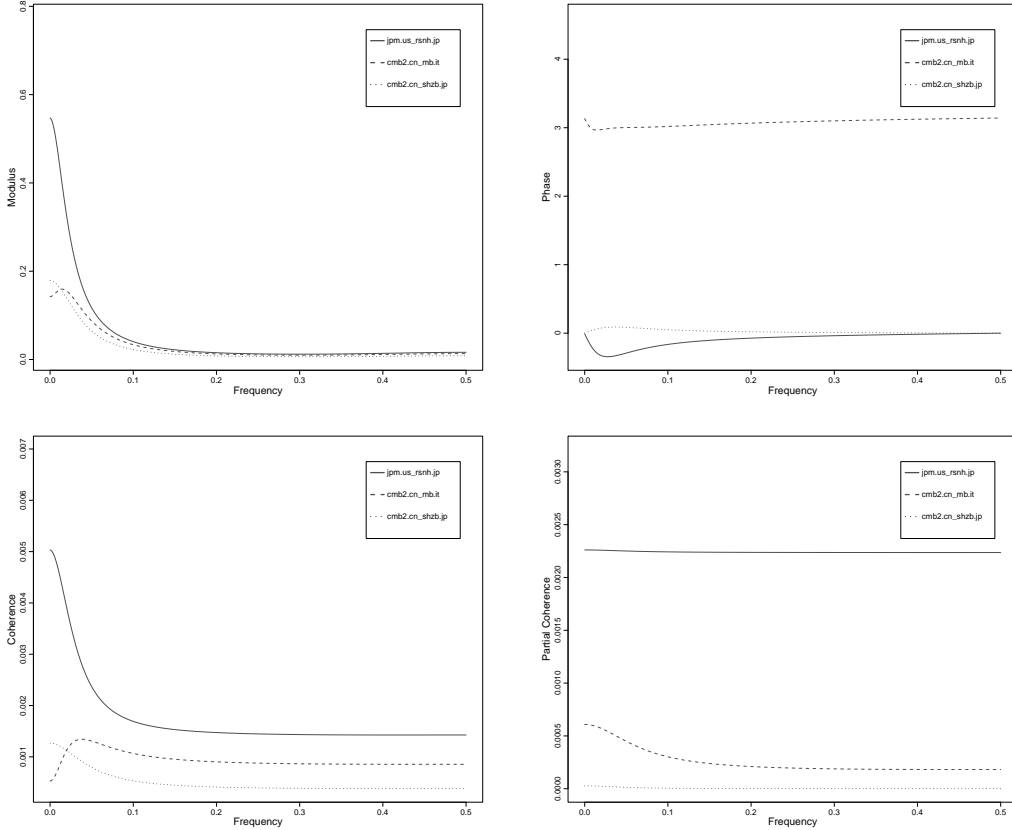


Figure D.4: Spectral summaries for three selected disconnected bank pairs (i, j) . Top row: modulus $|\hat{f}_{\text{GNAR}}(\cdot)|_{ij}$ and phase $\arg([\hat{f}_{\text{GNAR}}(\cdot)]_{ij})$ of estimated cross-spectra. Bottom row: squared coherence $[\hat{\rho}_{\text{GNAR}}(\cdot)]_{ij}^2$ and partial coherence $[\hat{\gamma}_{\text{GNAR}}(\cdot)]_{ij}^2$.